ORIGINAL ARTICLE

The free vibration analysis of hybrid porous nanocomposite joined hemispherical–cylindrical–conical shells

Emad Sobhani[1] · Arshia Arbabian[2] · Ömer Civalek[3] · Mehmet Avcar[4]

Abstract

In this research, the natural frequency responses of joined hemispherical–cylindrical–conical shells made of composite three-phase materials have been dealt with in the framework of First-Order Shear Deformation Theory (FOSDT). The joined hemispherical–cylindrical–conical shells are assumed to be made of hybrid porous nanocomposite material with three phases including a matrix of epoxy, macroscale carbon fiber, and nanoscale 3D Graphene Foams (3GFs). For getting the equivalent mechanical properties of the Hybrid Matrix (HM) including polymer epoxy and 3GFs, the well-known rule of the mixture is used. In addition, the effect of porosity throughout the HM is considered using two novel and one well-known porosity distribution pattern. Moreover, the HM is reinforced with transversely isotropic macroscale carbon fibers in which the Halpin–Tsai scheme is used for multiscale homogenization procedure. The governing equations of motion associated with hybrid porous nanocomposite joined hemispherical–cylindrical–conical structures are figured out by implementing Donnell-type shell formulation and Hamilton's approach. Moreover, an efficient and well-known semi-analytical solution method entitled Generalized Differential Quadrature Method (GDQM) is employed to solve the governing differential equations. To verify the proposed formulation some well-known benchmarks, especially those are composed of homogenous materials have been analyzed, and a good agreement has been achieved. Besides, some other new and applicable problems are considered to investigate the effects of different parameters including various boundary conditions, patterns of porosity distributions, and geometric properties of structure on the vibration behavior of joined shells.

1 Introduction

Shell structures are widely used in the engineering industry, some examples are pressure tanks, submarine and ship hulls, plane wings and hulls, pipes, outer surfaces of rockets, vehicle tires, reinforced concrete roofs, and liquid tanks. Hence, the shell structures having different geometric properties have extensively attracted the attention of many researchers in various fields of modern technology [1–22].

The vibration behavior of shell structures has been studied for several decades using many shell theories and formulations. The shell structures usually confront more complicated dynamic behaviors due to the curvature and thickness. Therefore, it is believable that axial constraints can be effective in the predominantly radial mode. Therefore, much research has been implemented to study the linear and nonlinear vibrations of homogenous and composite shell structures with different geometries. In addition, there are three different schemes including analytical, semi-analytical, and numerical to solve the governing equations. Among them, semi-analytical approaches have fascinated the interest of many researchers because of their higher potential and lower time and computational costs. To solve the complex Partial Differential Equations (PDEs), different numerical approximation methods are categorized into two

✉ Ömer Civalek
  Omer@mail.cmuh.org.tw

1 Department of Civil Engineering, Ferdowsi University of Mashhad, Mashhad, Iran

2 Department of Chemical Engineering, Ferdowsi University of Mashhad, Mashhad, Iran

3 Research Center for Interneural Computing, China Medical University, 40402 Taichung, Taiwan

4 Department of Civil Engineering, Suleyman Demirel University, 32260 Isparta, Turkey

approaches including numerical analysis and semi-analytical solutions. The Finite-Element Method and Finite-Difference technique are numerical analyses used for solving different complicated PDEs associated with various types of structure [23–28]. Due to the requirement of many elements or intervals in these approaches, the computational time is too high. Other techniques have been designed to minimize computing time by applying lesser meshes. Liew et al. [29] studied the free vibration of conical shells utilizing the Ritz method. Irie et al. [30] obtained the natural frequencies of conical shells with variable thickness. Civalek [31] proposed a discrete singular convolution method to investigate the vibration of rotating conical shells. Differential Quadrature Method (DQM), which is a special case of the finite difference method, is one of the most applicable semi-analytical solution methods for mechanical problems and it was introduced by Bellman et al. [32] for the first time. Then, Shu and Richards [33] overcame the drawbacks of DQM by proposing the Generalized Differential Quadrature Method (GDQM), which has been using by many researchers in different problems of engineering [34–37]. Du et al. [38] employed this method for structural analysis first and foremost. Shu [39] calculated the responses of conical shells employing GDQM. Bagheri et al. [40] used this efficient method for solving different PDEs of the free vibration problem of the conical shell. Moreover, the behavior of simple cylindrical shells with different boundary conditions was investigated numerically in various studies [41–43]. Furthermore, the buckling load and natural frequencies of conical shells with different boundary conditions were also investigated numerically in many other studies [44–50]. Lam et al. [51] analyzed the vibration of the truncated conical panels with different boundary conditions using GDQM. Hua and Lam [52, 53] used GDQM to implement the rotating effect on frequencies of conical shells. Viola and Artioli [54] used GDQM for the modal analysis of FSDT curved shells. Artioli and his coworkers [55, 56] examined the mechanical behaviors of the isotropic homogenous conical shells based on the Reissner–Mindlin hypothesis and applying GDQM.

Joined shells are alternative types of shell structures in which two or more shells with different geometries are coupled with each other. These types of structures have a wide range of applications in many fields of engineering, especially aerospace, mechanical, ocean, nuclear, and civil engineering. Irie et al. [57] presented the pioneer study on the free vibration analysis of joined conical–cylindrical shells. Kamat et al. [58] employed the principles of Bolotin's method for analyzing the laminated composite joined conical–cylindrical structures. Lee et al. [59] used Flugge shell theory and Rayleigh's energy method to obtain the vibration parameters of joined cylindrical–spherical shell structures. Wu et al. [60] determined the vibration characteristics of spherical–cylindrical–spherical structures applying Fourier series and Chebyshev polynomials displacement functions as admissible displacement fields in the framework of Reissner–Naghdi's thin shell theory. Bagheri et al. [61] utilized the GDQM for examining the natural frequencies of homogeneous joined conical–conical shells. Bagheri et al. [62] obtained the natural frequency of the coupled conical–cylindrical–conical shells implementing GDQM. Li et al. [63] studied the vibration of the coupled spherical–cylindrical structure applying the Ritz technique. Pang et al. [64] solved the governing equations of free vibration of spherical–cylindrical–spherical shells having arbitrary boundary conditions simulated with the penalty method using the Rayleigh–Ritz method. Rezaiee-Pajand et al. [65] reported the vibration parameters of functionally graded carbon nanotubes coupled with conical–conical shells employing the GDQM. Furthermore, numerical solutions have also been presented for these types of structures [66–68].

During recent decades, composite materials have been widely used in many structures of engineering because of their superior properties such as high strength and low weight. These advantages attracted the attention of several researchers to study the mechanical behaviors of composite structures having different geometries in micro/macro scales [69–73]. Composites can be manufactured in several ways, one of these ways is the construction of isotropic-nonhomogeneous composite having three parts two nano- and a macro-scale material. These phases include a matrix is made of polymer, macro-, and nano-measure fibers. The mixture of polymer matrix and nanoscale fiber augmentation is identified as Hybrid Matrix (HM). Rafiee et al.[74] performed geometrically nonlinear analysis of plates made of hybrid nanocomposite piezoelectric materials in the framework of the first shear deformation theory. Ebrahimi and Habibi [75] investigated the nonlinear thermomechanical behavior of hybrid nanocomposite plates using the multiscale method. Gholami and Ansari [76] studied the nonlinear bending behavior of multiscale hybrid nanocomposite plates adopting von Kármán principles. Dabbagh et al. [77] obtained the natural frequencies of multiscale hybrid nanocomposite beams using the Finite-Element Method (FEM). Karimiasl et al. [78] performed the dynamic hygro-thermomechanical analysis of doubly curved structures made of hybrid nanocomposite materials. The production of nanocomposites involves several complex steps, and some technical problems may be met in the manufacturing process of nanocomposites that cause porosity. The presence of porosities inside nanocomposites results in the decrease of the strength of the material. Therefore, the examination of the effect of porosity on the structures is a major issue [79–85].

As a result of the search of open literature, it is seen that the vibration of joined hemispherical–cylindrical–conical shells composed of hybrid porous nanocomposite materials has not been studied yet. Especially, the effects of the use

of distinct types of composite materials and various multiscale homogenization approaches have not been investigated. Besides, three-phase hybrid nanocomposite materials in many structures, especially shell-like structures still need to be developed numerically, while the stated issue can be solved using an efficient semi-analytical solution method of GDQM. For this context, the free vibration analysis of hybrid porous nanocomposite joined hemispherical–cylindrical–conical composite shells is examined using a semi-analytical solution approach in this paper. First, the considered hybrid porous nanocomposite material, i.e., a three-phase composite material is made of two main parts including Hybrid Matrix (HM) and transversely isotropic macroscale AS4 carbon fiber, is defined, and the related formulations are obtained. Namely, parts of the composite shell are homogenized using the well-known Halpin–Tsai multiscale approach, as well as the rule of mixture method is employed to obtain the equivalent mechanical properties of HM, which is manufactured by 3502-epoxy polymer and nanoscale 3D Graphene Foams (3GFs). After figuring out the equivalent mechanical and physical attributes to the three-phase material, the governing equations of motion of joined composite shell are derived applying Donnell's shell theory and Hamilton's principles. Then, the governing differential equations of motion are numerically solved using the well-known semi-analytical method of GDQM. The solution procedure is completely presented. A computer program is developed using this procedure to unravel the diverse complex and enforceable moot points. Finally, several examinations are considered to confirm the given formulation and procedure. Further, some other new, complex, and applicable joined shell problems with different geometric, material, and boundary conditions are examined to affirm the authenticity, accuracy, and sufficiency of the recommended formulation as well.

2 The properties of the Hybrid Matrix

HM are manufactured in two parts including polymer and nanofiller synthesizers. In this study, the polymeric 3502-epoxy resin is utilized for the polymer part of HM material [86]. Nanofiller materials are classified into several types, and 3D Graphene Foam (3GF) is one of the nanofillers that can be used in hybrid materials. In addition, the 3GFs enhance the performance and mechanical properties of HM materials.

The equivalent mechanical properties of HM are figured out by utilizing the well-known rule of the mixture as follows:

$$E_{HM}^0 = E_m(1 - V_{Gr}) + E_{Gr}V_{Gr} \tag{1}$$

$$\rho_{HM}^0 = \rho_m(1 - V_{Gr}) + \rho_{Gr}V_{Gr} \tag{2}$$

$$\nu_{HM}^0 = \nu_m(1 - V_{Gr}) + \nu_{Gr}V_{Gr}, \tag{3}$$

where E_m, E_{Gr}, and E_{HM}^0 represent Young's modulus of the matrix, 3GFs, and HM, respectively. Besides, the density of HM, matrix, and 3GFs are shown with ρ_{HM}^0, ρ_m and ρ_{Gr}, respectively. On the other hand, ν_{HM}^0, ν_m and ν_{Gr} represent Poisson's ratio of HM, matrix, and 3GFs, respectively.

The volume fraction of 3GFs is calculated as follows:

$$V_{Gr} = \frac{w_{Gr}}{w_{Gr} + (\rho_{Gr}/\rho_m) - w_{Gr}(\rho_{Gr}/\rho_m)}, \tag{4}$$

where w_{Gr} defines the weight fraction of 3GFs.

Note that the total volume fraction of 3GFs and matrix is equal to one based on the rule of mixture ($V_{Gr} + V_m = 1$).

The shear module of HM is found as follows:

$$G_{HM}^0 = \frac{E_{HM}^0}{2(1 + \nu_{HM}^0)}. \tag{5}$$

In this study, three different patterns are used to demonstrate the distribution of porosity in 3GFs and polymers constructing HM material. These porosity skeleton forms are defined as pattern-I, pattern-II, and pattern-III [87–89].

It is worthy to mention that the mechanical properties of HM are influenced by the porosity distribution along with the thickness of the structure.

To determine the mechanical properties of HM regarding porosity pattern-I, the following expressions can be given as follows:

$$E_{HM}^{I}(\eta) = E_{HM}^0 \left[1 - \xi_I \cos\left(\frac{\pi\eta}{h}\right) \right] \tag{6}$$

$$G_{HM}^{I}(\eta) = G_{HM}^0 \left[1 - \xi_I \cos\left(\frac{\pi\eta}{h}\right) \right] \tag{7}$$

$$\rho_{HM}^{I}(\eta) = \rho_{HM}^0 \left[1 - \mu_I \cos\left(\frac{\pi\eta}{h}\right) \right], \tag{8}$$

where Young's and shear modulus, and density of porous HM using pattern-I are defined as E_{HM}^{I}, G_{HM}^{I}, and ρ_{HM}^{I}, respectively. Moreover, ξ_I and μ_I are Young's modulus and density factors of porosity about pattern-I.

Figure 1 depicts the variation of Young's modulus and density of porous HM according to pattern-I along the thickness direction.

The mechanical and physical properties of HM according to the pattern-II distribution of porosity along the thickness can be given as follows:
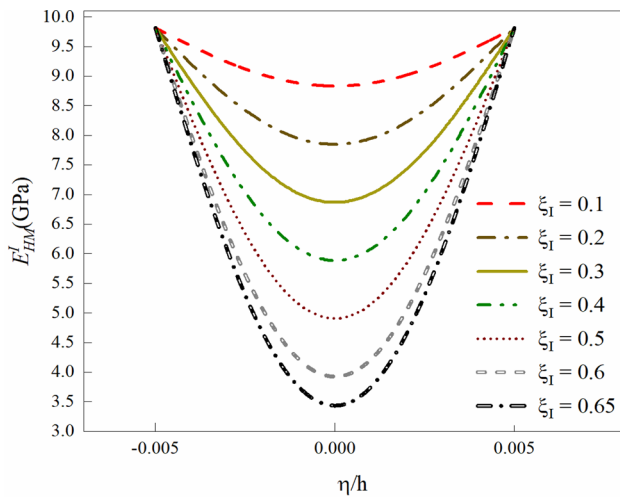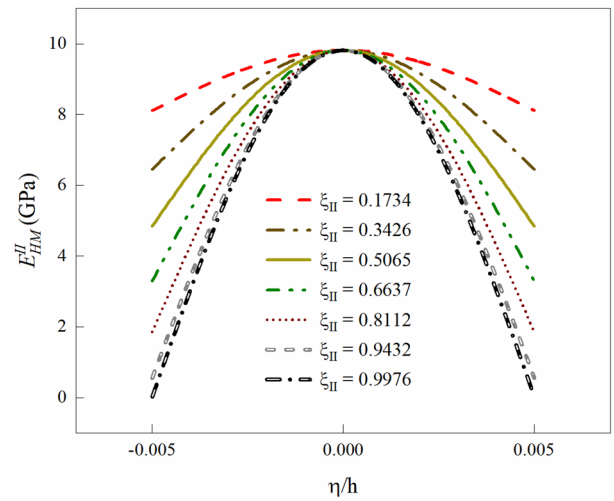
(a)
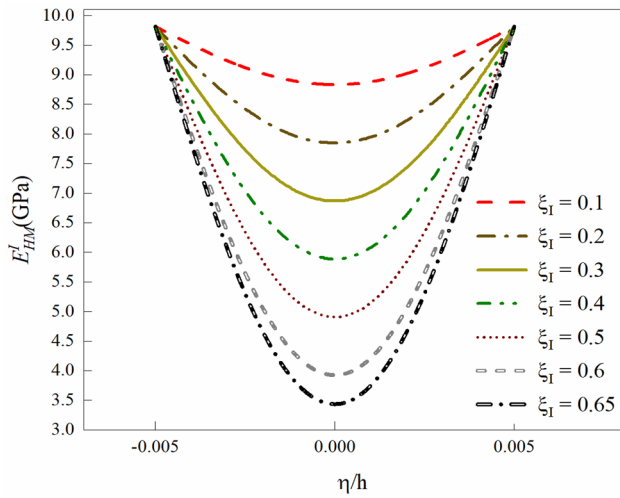
(b)

Fig. 1 The variation of (**a**) Young's modulus and (**b**) density of porous HM according to pattern-I along the thickness direction

(a)

(b)

Fig. 2 The variation of (**a**) Young's modulus and (**b**) density of porous HM according to pattern-II along the thickness direction

The variation of Young's modulus and density of HM including porosity according to the pattern-II along the thickness is illustrated in Fig. 2.

The mechanical and physical properties of porous HM according to the pattern-III distribution of porosity can be given as follows:

$$E_{HM}^{II}(\eta) = E_{HM}^0 \left\{ 1 - \xi_{II} \left[1 - \cos\left(\frac{\pi\eta}{h}\right) \right] \right\} \quad (9)$$
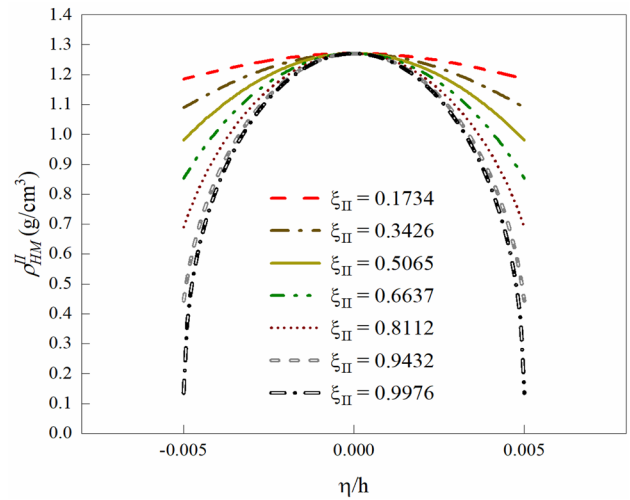
$$G_{HM}^{II}(\eta) = G_{HM}^0 \left\{ 1 - \xi_{II} \left[1 - \cos\left(\frac{\pi\eta}{h}\right) \right] \right\} \quad (10)$$

$$\rho_{HM}^{II}(\eta) = \rho_{HM}^0 \left\{ 1 - \mu_{II} \left[1 - \cos\left(\frac{\pi\eta}{h}\right) \right] \right\}, \quad (11)$$

where E_{HM}^{II}, G_{HM}^{II} and ρ_{HM}^{II}, respectively, represent the Young's and shear modulus, and density of porous HM about the pattern-II. The factors of Young's modulus and density for the pattern-II are defined with ξ_{II} and μ_{II}, respectively.

$$E_{HM}^{III} = E_{HM}^0 \xi_{III} \quad (12)$$

$$G_{HM}^{III} = G_{HM}^0 \xi_{III} \quad (13)$$

$$\rho_{HM}^{III} = \rho_{HM}^0 \mu_{III}. \quad (14)$$

The variation of Young's modulus and density of HM including porosity according to the pattern-III along the thickness is illustrated in Fig. 3.

The relation between Young's modulus of HM and porous HM with the density of HM and porous HM for each pattern of porosity distribution can be found with the following expression [90–93]:

$$\frac{E^i_{HM}(z)}{E^0_{HM}} = \left(\frac{\rho^i_{HM}(z)}{\rho^0_{HM}} \right)^{2.73} \quad \text{for } i = \text{I, II, III} \tag{15}$$

On the other hand, the relation between the elastic modulus and density factors in each pattern of porosity distribution can be found as follows:

$$\begin{bmatrix} 1 - \mu_{\text{I}} \cos\left(\frac{\pi z}{h}\right) = \sqrt[2.73]{1 - \xi_{\text{I}} \cos\left(\frac{\pi z}{h}\right)} & \text{Pattern} - \text{I} \\ 1 - \mu_{\text{II}} \left\{ 1 - \cos\left(\frac{\pi z}{h}\right) \right\} = \sqrt[2.73]{1 - \xi_{\text{II}} \left\{ 1 - \cos\left(\frac{\pi z}{h}\right) \right\}} & \text{Pattern} - \text{II} \\ \mu_{\text{III}} = \sqrt[2.73]{\xi_{\text{III}}} & \text{Pattern} - \text{III} \end{bmatrix} \tag{16}$$

In addition, the relations between Young's modulus factors of each pattern of porosity distribution with the other can be determined as follows:

$$\begin{bmatrix} \int_0^{\frac{h}{2}} \sqrt[2.73]{1 - \xi_{\text{II}} \left\{ 1 - \cos\left(\frac{\pi z}{h}\right) \right\}} \, dz = \int_0^{\frac{h}{2}} \sqrt[2.73]{1 - \xi_{\text{I}} \cos\left(\frac{\pi z}{h}\right)} \, dz \\ \int_0^{\frac{h}{2}} \sqrt[2.73]{\xi_{\text{III}}} \, dz = \int_0^{\frac{h}{2}} \sqrt[2.73]{1 - \xi_{\text{I}} \cos\left(\frac{\pi z}{h}\right)} \, dz \end{bmatrix} \tag{17}$$

Table 1 reports the values of Young's modulus factors of all three patterns versus Eq. (17). It is observed that the values of ξ_{II} enhanced with the increasing the values of ξ_I, and the values of ξ_{II} tends to (~ 1). The domain of ξ_I is assigned to be $[0, 0.65]$.

The mechanical properties of 3D Graphene Foams and 3506-epoxy resin materials are reported in Table 2.

3 Homogenization of HM with AS4 carbon fibers

The special type of materials is formed in three phases by mixing polymeric matrix, macro-filler fiber, and micro-filler 3GFs. Therefore, HM material can be reinforced with fibers. In addition, HM material is reinforced with the use of macroscale particles which can improve the mechanical properties of HM. Multiscale analysis can be used to find the effective mechanical properties of this type of material. The
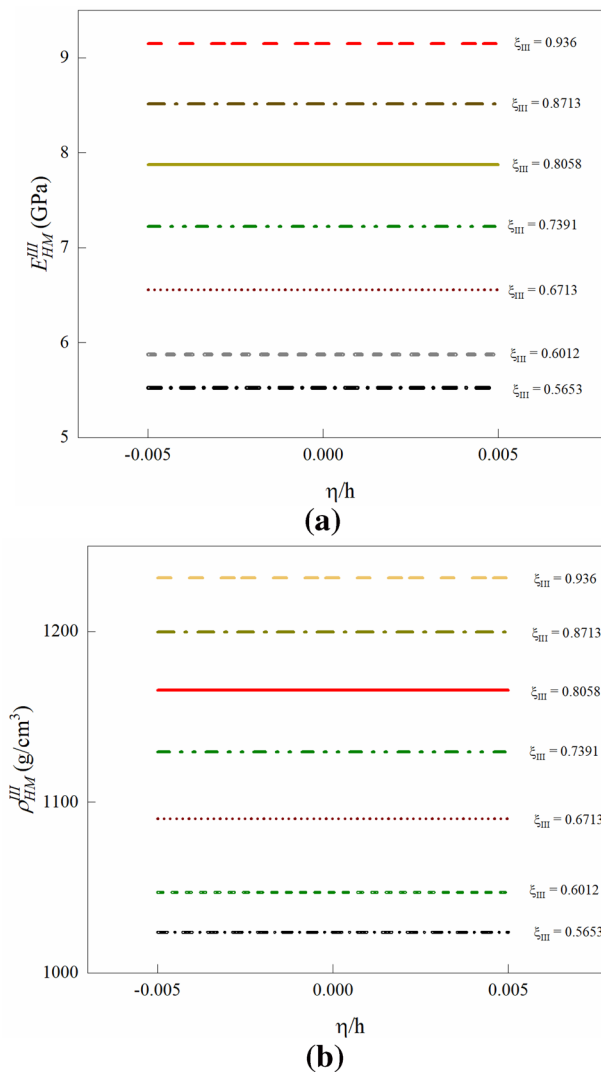

Fig. 3 The variation of (**a**) Young's modulus and (**b**) density of porous HM according to pattern-III along the thickness direction

Table 1 The coefficient of porosity patterns

ξ_I	ξ_{II}	ξ_{III}
0.1	0.1734	0.9360
0.2	0.3426	0.8713
0.3	0.5065	0.8085
0.4	0.6637	0.7391
0.5	0.8112	0.6711
0.6	0.9432	0.6012
0.65	0.9976	0.5653

Table 2 The mechanical properties of nanofiller and matrix materials

Material	E(Gpa)	v	ρ(kg/m^3)
3D Graphene Foams	1020	0.3	2300
3501-6 epoxy resin (Matrix)	4.2	0.34	1265

mechanical properties of the fibers can be categorized into three groups of isotropic, transversely isotropic, and anisotropic materials. Transversely isotropic AS4 carbon fibers have continuous, high strength, high strain, and PAN-based properties. Therefore, it can be employed for improving the behavior of HM materials [86]. Based on this, Young's modulus of transversely isotropic fiber can be assumed to be $E^1_{\text{fiber}}, E^2_{\text{fiber}} = E^3_{\text{fiber}}$. In addition, the shear modulus of this group is represented with $G^{23}_{\text{fiber}}, G^{12}_{\text{fiber}} = G^{13}_{\text{fiber}}$. Furthermore, $v^{12}_{\text{fiber}} = v^{13}_{\text{fiber}}, v^{23}_{\text{fiber}}$ represent Poisson's ratio of transversely isotropic fibers.

There are many multiscale techniques, Halpin–Tsai is one of these methods which is employed in this research to evaluate the equivalent three-phase material mechanical properties. On the other hand, the Halpin–Tsai homogenization approach determines the mechanical properties of three-phase materials by utilizing Hill's Young's modulus parameters [94–98].

Appropriately, Hill's parameters of HM material are calculated as follows:

$$m_{\text{fiber}} = \frac{E^2_{\text{fiber}}}{2(1 + v^{23}_{\text{fiber}})} = \frac{1 - v^{23}_{\text{fiber}} - 2v^{21}_{\text{fiber}}v^{12}_{\text{fiber}}}{1 + v^{23}_{\text{fiber}}}k_{\text{fiber}} \tag{25}$$

$$n_{\text{fiber}} = \frac{E^1_{\text{fiber}}(1 - v^{23}_{\text{fiber}})}{1 - v^{23}_{\text{fiber}} - 2v^{21}_{\text{fiber}}v^{12}_{\text{fiber}}} = 2(1 - v^{23}_{\text{fiber}})\frac{E^1_{\text{fiber}}}{E^2_{\text{fiber}}}k_{\text{fiber}} \tag{26}$$

$$p_{\text{fiber}} = G^{12}_{\text{fiber}}. \tag{27}$$

In addition, the effective Hill's parameters in terms of HM and AS4 carbon fibers are obtained as follows:

$$k_{\text{eff}} = \frac{k_{HM}(k_{\text{fiber}} + m_{HM})(1 - V_{\text{fiber}}) + k_{\text{fiber}}(k_{HM} + m_{HM})V_{\text{fiber}}}{(k_{\text{fiber}} + m_{HM})(1 - V_{\text{fiber}}) + (k_{HM} + m_{HM})V_{\text{fiber}}} \tag{28}$$

$$l_{\text{eff}} = V_{\text{fiber}}l_{\text{fiber}} + (1 - V_{\text{fiber}})$$
$$+ \frac{l_{\text{fiber}} - l_{HM}}{k_{\text{fiber}} - k_{HM}}(k_{\text{eff}} - V_{\text{fiber}}k_{\text{fiber}} - (1 - V_{\text{fiber}})k_{HM}) \tag{29}$$

$$m_{\text{eff}} = m_{HM}\frac{2V_{\text{fiber}}m_{\text{fiber}}(k_{HM} + m_{HM}) + 2(1 - V_{\text{fiber}})m_{\text{fiber}}m_{HM} + (1 - V_{\text{fiber}})k_{HM}(m_{\text{fiber}} + m_{HM})}{2V_{\text{fiber}}m_{HM}(k_{HM} + m_{HM}) + 2(1 - V_{\text{fiber}})m_{\text{fiber}}m_{HM} + (1 - V_{\text{fiber}})k_{HM}(m_{\text{fiber}} + m_{HM})} \tag{30}$$

$$k_{HM} = \frac{E^i_{HM}}{2(1 - v^0_{HM} - 2(v^0_{HM})^2)} \quad \text{for } i = \text{I, II, III} \tag{18}$$

$$l_{HM} = \frac{v^0_{HM}E^i_{HM}}{(1 - v^0_{HM} - 2(v^0_{HM})^2)} = 2v^0_{HM}k_{HM} \quad \text{for } i = \text{I, II, III} \tag{19}$$

$$m_{HM} = G^i_{HM} = \frac{E^i_{HM}}{2(1 + v^0_{HM})} = (1 - 2v^0_{HM})k_{HM} \quad \text{for } i = \text{I, II, III} \tag{20}$$

$$n_{HM} = \frac{(1 - v^0_{HM})E^i_{HM}}{(1 - v^0_{HM} - 2(v^0_{HM})^2)} = 2(1 - v^0_{HM})k_{HM} \quad \text{for } i = \text{I, II, III} \tag{21}$$

$$p_{HM} = G^i_{HM} = (1 - 2v^0_{HM})k_{HM} = m_{HM} \quad \text{for } i = \text{I, II, III}. \tag{22}$$

On the other hand, Hill's factors of transversely isotropic AS4 carbon fiber are given as follows:

$$k_{\text{fiber}} = \frac{E^2_{\text{fiber}}}{2(1 - v^{23}_{\text{fiber}} - 2v^{21}_{\text{fiber}}v^{12}_{\text{fiber}})} \tag{23}$$

$$l_{\text{fiber}} = \frac{v^{12}_{\text{fiber}}E^2_{\text{fiber}}}{(1 - v^{23}_{\text{fiber}} - 2v^{21}_{\text{fiber}}v^{12}_{\text{fiber}})} = 2v^{12}_{\text{fiber}}k_{\text{fiber}} \tag{24}$$

$$n_{\text{eff}} = V_{\text{fiber}}n_{\text{fiber}} + (1 - V_{\text{fiber}})n_{HM}$$
$$+ \left(\frac{l_{\text{fiber}} - l_{HM}}{k_{\text{fiber}} - k_{HM}}\right)^2(k_{\text{eff}} - V_{\text{fiber}}k_{\text{fiber}} - (1 - V_{\text{fiber}})k_{HM}) \tag{31}$$

$$p_{\text{eff}} = \frac{(p_{\text{fiber}} + p_{HM})p_{HM}(1 - V_{\text{fiber}}) + 2p_{\text{fiber}}p_{HM}V_{\text{fiber}}}{(p_{\text{fiber}} + p_{HM})(1 - V_{\text{fiber}}) + 2p_{HM}V_{\text{fiber}}}$$
$$p_{\text{fiber}} = G^{12}_{\text{fiber}}. \tag{32}$$

The effective mechanical properties of three-phase material are determined employing the Halpin–Tsai approach with the following expressions:

$$E^{\text{eff}}_1 = E^1_{\text{fiber}}V_{\text{fiber}} + E^i_{Hm}(1 - V_{\text{fiber}}) \quad \text{for } i = \text{I, II, III} \tag{33}$$

$$E^{\text{eff}}_2 = \frac{4(n_{\text{eff}}k_{\text{eff}} - l^2_{\text{eff}})m_{\text{eff}}}{(k_{\text{eff}} + m_{\text{eff}})n_{\text{eff}} - l^2_{\text{eff}}} \tag{34}$$

$$v^{\text{eff}}_{12} = v^{12}_{\text{fiber}}V_{\text{fiber}} + v^0_{Hm}(1 - V_{\text{fiber}}) \tag{35}$$

$$G^{12}_{\text{eff}} = G^{13}_{\text{eff}} = p_{\text{eff}} \tag{36}$$

$$G^{23}_{\text{eff}} = m_{\text{eff}} \tag{37}$$

$$\rho_{\text{eff}} = \rho_{\text{fiber}}V_{\text{fiber}} + \rho^i_{Hm}(1 - V_{\text{fiber}}) \quad \text{for } i = \text{I, II, III}. \tag{38}$$

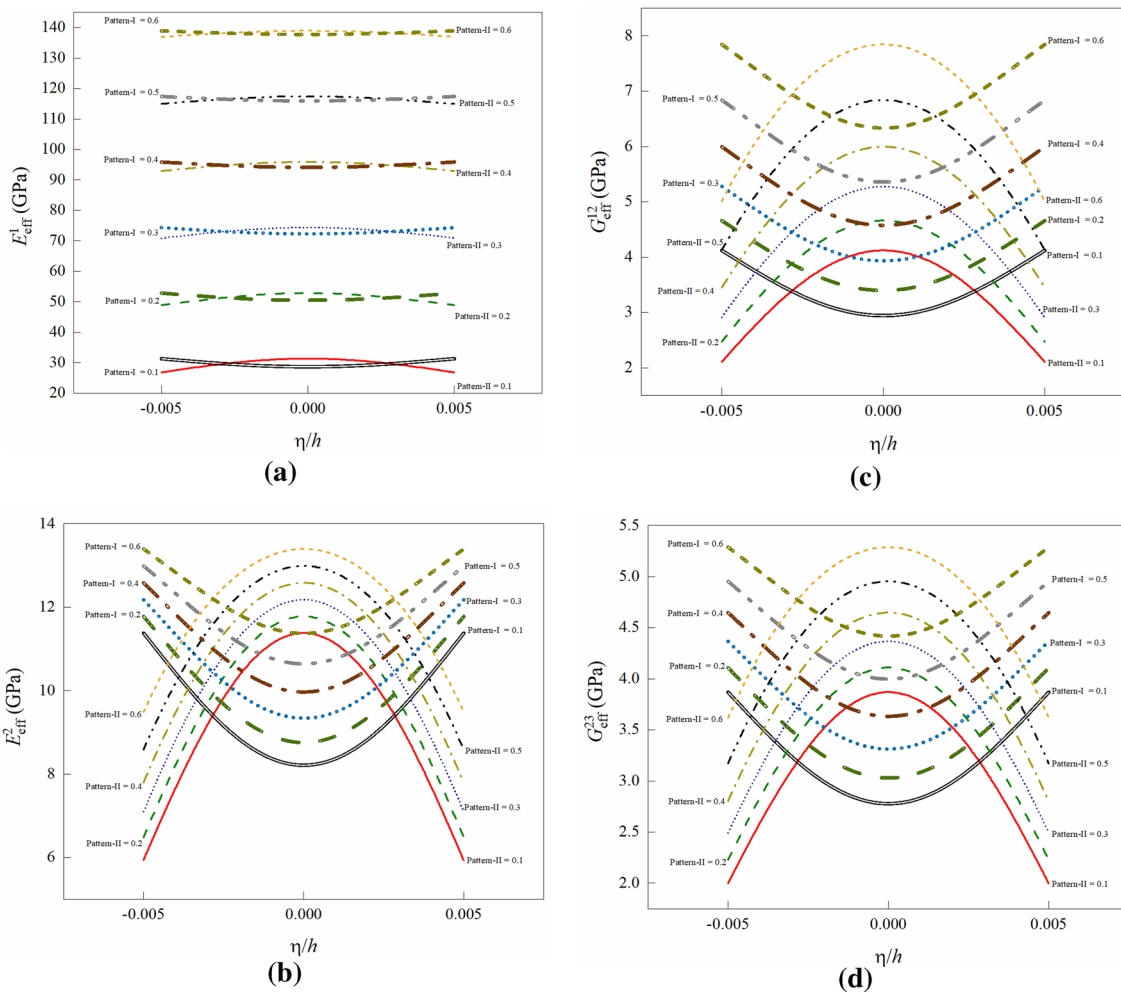The mechanical properties of the transversely isotropic AS4 carbon fibers material are reported in Table 3.

The variation of engineering constants of 3506-epoxy resin-AS4 carbon fibers-3D Graphene Foams three-phase material along the thickness direction of the joined shell is illustrated in Fig. 4 for two different patterns of porosity.

4 The fundamental relations and expressions

One of the most applicable shells is joined shell structures due to their superior performance and high proficiency, and the joined hemispherical–cylindrical–conical structure is one of these structures. The joined shells have wide applications in aerospace, mechanics, and civil engineering. On the

Table 3 The mechanical properties of carbon fiber material

Material	E_{fiber}^1 (GPa)	E_{fiber}^2 (GPa)	v_{fiber}^{12}	v_{fiber}^{23}	G_{fiber}^{12} (GPa)	ρ_{fiber} (kg/m^3)
AS4 Carbon fiber	225.0	15.0	0.2	0.07	15.0	1790

Fig. 4 The variation of equivalent mechanical properties along the thickness direction of joined shell, (**a**) longitudinal Young's modulus, (**b**) transverse Young's modulus, (**c**) in-plane shear modulus, (**d**) out-of-plane shear modulus

other hand, employing new forms of materials such as three-phase hybrid matrix nanocomposite materials can improve the behavior of these serviceable structures as well.

Figure 5 depicts the paradigm of nanocomposite three-phase hybrid porous joined hemispherical–cylindrical–conical shell.

In this work, the FOSDT and Donnell's shell theory are employed to solve the joined hemispherical–cylindrical–conical shell formulation. Therefore, the displacement field of this structure is found as follows:

$$U_1^i(\zeta_i, \theta, \eta, t) = u_1^i(\zeta_i, \theta, t) + \eta \Psi_\zeta^i(\zeta_i, \theta, t)$$
$$U_2^i(\zeta_i, \theta, \eta, t) = u_2^i(\zeta_i, \theta, t) + \eta \Psi_\theta^i(\zeta_i, \theta, t) \text{ for } i = co, cy, hs$$
$$U_3^i(\zeta_i, \theta, \eta, t) = u_3^i(\zeta_i, \theta, t).$$

(39)

where U_1^i, U_2^i, U_3^i define the hemispherical–cylindrical–conical shell displacements in various directions, respectively. In addition, the mid-surface displacements along the directions of ζ_i, θ, η are represented by u_1^i, u_2^i, u_3^i, respectively. $\Psi_\zeta^i, \Psi_\theta^i$ are the mid-surface transversely normal rotations about θ, ζ_i directions, respectively. The axes of the

Fig. 5 The scheme of HM-carbon fiber nanocomposite joined hemispherical–cylindrical–conical shell structure
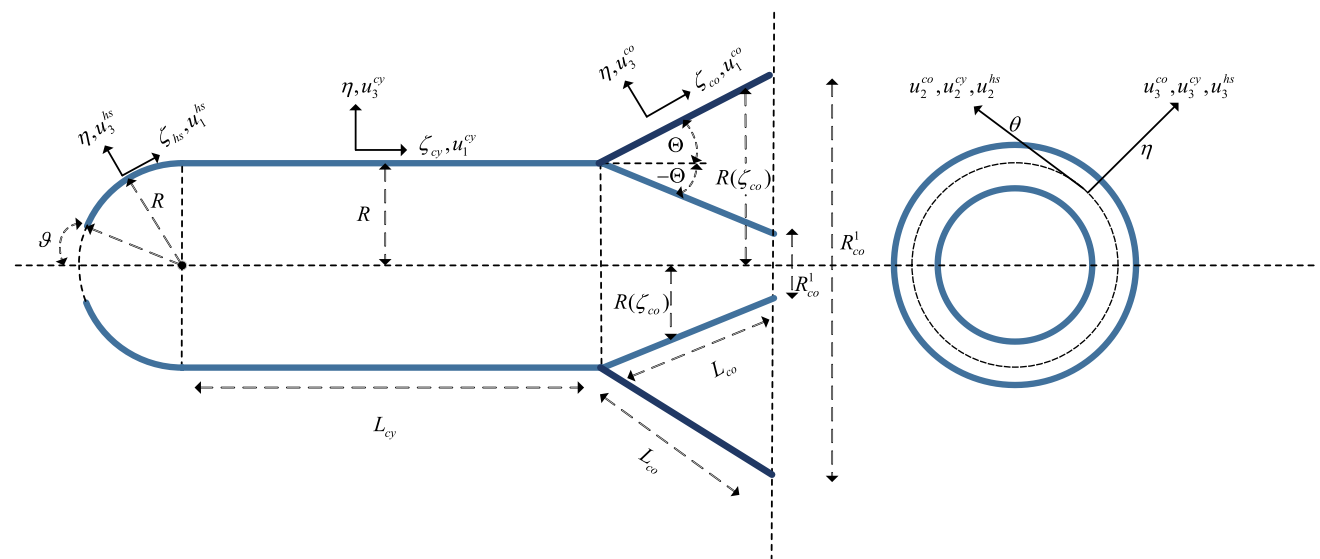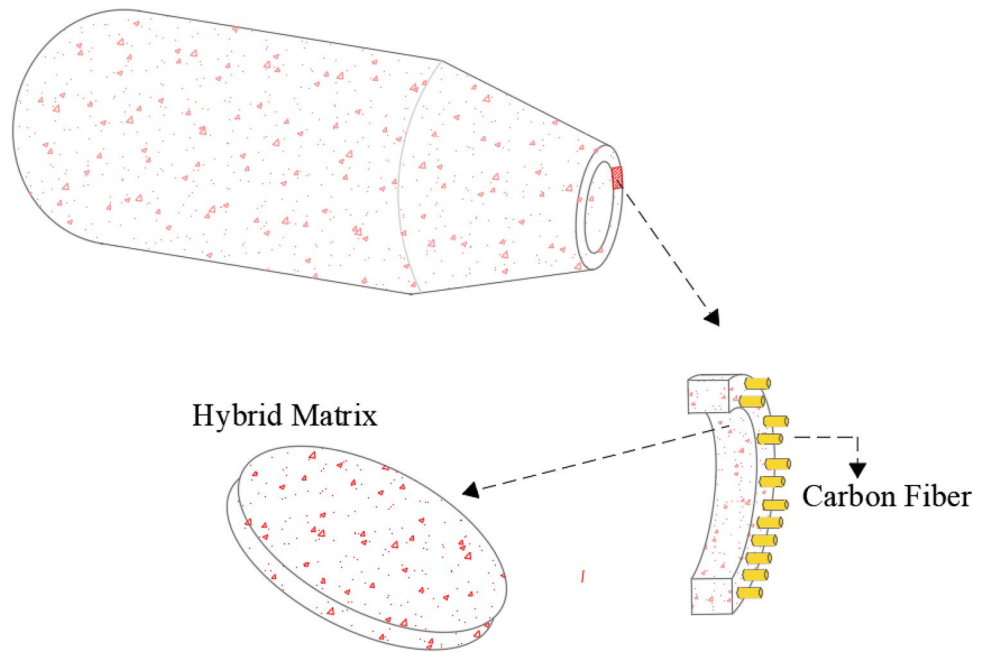
Fig. 6 The geometrical characteristics of joined hemispherical–cylindrical–conical shells

longitudinal, circumferential, and normal directions of the hemispherical–cylindrical–conical shells defined at the mid-surface are indicated with ζ_i, θ, η, respectively. The longitudinal directions for cylindrical and conical parts of this structure are defined $0 \leq \zeta_{cy} \leq L_{cy}, 0 \leq \zeta_{co} \leq L_{co}$ while $\vartheta \leq \zeta_{hs} \leq \frac{\pi}{2}$ is used for the domain of longitudinal direction of hemispherical one. Accordingly, the geometrical properties of joined hemispherical–cylindrical–conical shell structure are shown in Fig. 6.

The strain fields of hemispherical, cylindrical, and conical shells in terms of mid-surface strains and curvatures are found utilizing Donnell's approach and FSDT as follows:

$$\begin{Bmatrix} \varepsilon_\zeta^i \\ \varepsilon_\theta^i \\ \gamma_{\zeta\theta}^i \\ \gamma_{\zeta\eta}^i \\ \gamma_{\theta\eta}^i \end{Bmatrix} = \begin{Bmatrix} \bar{\varepsilon}_\zeta^i \\ \bar{\varepsilon}_\theta^i \\ \bar{\gamma}_{\zeta\theta}^i \\ \bar{\gamma}_{\zeta\eta}^i \\ \bar{\gamma}_{\theta\eta}^i \end{Bmatrix} + \eta \begin{Bmatrix} \chi_\zeta^i \\ \chi_\theta^i \\ \chi_{\zeta\theta}^i \\ \chi_{\zeta\eta}^i \\ \chi_{\theta\eta}^i \end{Bmatrix} \text{ for } i = co,cy,hs, \quad (40)$$

where $\bar{\varepsilon}_\zeta^i, \bar{\varepsilon}_\theta^i$ indicate the normal strains of mid-surface along with ζ_i, θ directions, respectively, while an in-plane shear strain is defined by $\bar{\gamma}_{\zeta\theta}^i$. $\bar{\gamma}_{\zeta\eta}^i, \bar{\gamma}_{\theta\eta}^i$ represent the out-of-plane shear strains. The curvatures of each part of the hemispherical–cylindrical–conical are depicted with $\chi_\zeta^i, \chi_\theta^i, \chi_{\zeta\theta}^i, \chi_{\zeta\eta}^i, \chi_{\theta\eta}^i$, respectively. The relation between strains and displacements of mid-surface of the cylindrical part of joined hemispherical–cylindrical–conical can be found employing Donnell's shell theory and FOSDT as follows:

$$\begin{Bmatrix} \bar{\varepsilon}_\zeta^{cy} \\ \bar{\varepsilon}_\theta^{cy} \\ \bar{\gamma}_{\zeta\theta}^{cy} \\ \bar{\gamma}_{\zeta\eta}^{cy} \\ \bar{\gamma}_{\theta\eta}^{cy} \end{Bmatrix} = \begin{Bmatrix} \dfrac{\partial u_1^{cy}}{\partial \zeta_{cy}} \\[2mm] \dfrac{1}{R_{cy}}\dfrac{\partial u_2^{cy}}{\partial\theta} + \dfrac{u_3^{cy}}{R_{cy}} \\[2mm] \dfrac{\partial u_2^{cy}}{\partial \zeta_{cy}} + \dfrac{1}{R}\dfrac{\partial u_1^{cy}}{\partial\theta} \\[2mm] \dfrac{\partial u_3^{cy}}{\partial \zeta_{cy}} + \Psi_\zeta^{cy} \\[2mm] \dfrac{1}{R}\dfrac{\partial u_3^{cy}}{\partial\theta} - \dfrac{u_2^{cy}}{R} + \Psi_\theta^{cy} \end{Bmatrix}. \quad (41)$$

On the other hand, the above relation can be re-written in the form of the conical part as follows:

$$\begin{Bmatrix} \bar{\varepsilon}_\zeta^{co} \\ \bar{\varepsilon}_\theta^{co} \\ \bar{\gamma}_{\zeta\theta}^{co} \\ \bar{\gamma}_{\zeta\eta}^{co} \\ \bar{\gamma}_{\theta\eta}^{co} \end{Bmatrix} = \begin{Bmatrix} \dfrac{\partial u_1^{co}}{\partial \zeta_{co}} \\[2mm] \dfrac{1}{R(\zeta_{co})}\dfrac{\partial u_2^{co}}{\partial\theta} + \dfrac{\sin(\Theta)}{R(\zeta_{co})}u_1^{co} + \dfrac{\cos(\Theta)}{R(\zeta_{co})}u_3^{co} \\[2mm] \dfrac{\partial u_2^{co}}{\partial \zeta_{co}} + \dfrac{1}{R(\zeta_{co})}\dfrac{\partial u_1^{co}}{\partial\theta} - \dfrac{\sin(\Theta)}{R(\zeta_{co})}u_2^{co} \\[2mm] \dfrac{\partial u_3^{co}}{\partial \zeta_{co}} + \Psi_\zeta^{co} \\[2mm] \dfrac{1}{R(\zeta_{co})}\dfrac{\partial u_3^{co}}{\partial\theta} - \dfrac{\cos(\Theta)}{R(\zeta_{co})}u_2^{co} + \Psi_\theta^{co} \end{Bmatrix}. \quad (42)$$

Conversely, the hemispherical part mid-surface strain and displacement relations can be figured out as follows:

$$\begin{Bmatrix} \bar{\varepsilon}_\zeta^{hs} \\ \bar{\varepsilon}_\theta^{hs} \\ \bar{\gamma}_{\zeta\theta}^{hs} \\ \bar{\gamma}_{\zeta\eta}^{hs} \\ \bar{\gamma}_{\theta\eta}^{hs} \end{Bmatrix} = \begin{Bmatrix} \dfrac{1}{R}\dfrac{\partial u_1^{hs}}{\partial \zeta_{hs}} + \dfrac{u_3^{hs}}{R} \\[2mm] \dfrac{1}{R\sin(\zeta_{hs})}\dfrac{\partial u_2^{hs}}{\partial\theta} + \dfrac{\cot(\zeta_{hs})}{R}u_1^{hs} + \dfrac{u_3^{hs}}{R} \\[2mm] \dfrac{1}{R}\dfrac{\partial u_2^{hs}}{\partial \zeta_{hs}} + \dfrac{1}{R\sin(\zeta_{hs})}\dfrac{\partial u_1^{hs}}{\partial\theta} - \dfrac{\cot(\zeta_{hs})}{R}u_2^{hs} \\[2mm] \dfrac{1}{R}\dfrac{\partial u_3^{hs}}{\partial \zeta_{hs}} + \Psi_\zeta^{hs} - \dfrac{u_1^{hs}}{R} \\[2mm] \dfrac{1}{R\sin(\zeta_{hs})}\dfrac{\partial u_3^{hs}}{\partial\theta} - \dfrac{u_2^{hs}}{R} + \Psi_\theta^{hs} \end{Bmatrix}. \quad (43)$$

The relation between the curvatures and mid-surface displacements of cylindrical part can be expressed using Donnell's shell theory and FOSDT as follows:

$$\begin{Bmatrix} \chi_\zeta^{cy} \\ \chi_\theta^{cy} \\ \chi_{\zeta\theta}^{cy} \\ \chi_{\zeta\eta}^{cy} \\ \chi_{\theta\eta}^{cy} \end{Bmatrix} = \begin{Bmatrix} \dfrac{\partial\Psi_\zeta^{cy}}{\partial\zeta_{cy}} \\[2mm] \dfrac{1}{R}\dfrac{\partial\Psi_\theta^{cy}}{\partial\theta} \\[2mm] \dfrac{\partial\Psi_\theta^{cy}}{\partial\zeta_{cy}} + \dfrac{1}{R}\dfrac{\partial\Psi_\zeta^{cy}}{\partial\theta} \\[2mm] 0 \\[2mm] 0 \end{Bmatrix}. \quad (44)$$

Based on these assumptions, the above relation can be re-written for the conical part as follows:

$$\begin{Bmatrix} \chi_\zeta^{co} \\ \chi_\theta^{co} \\ \chi_{\zeta\theta}^{co} \\ \chi_{\zeta\eta}^{co} \\ \chi_{\theta\eta}^{co} \end{Bmatrix} = \begin{Bmatrix} \dfrac{\partial\Psi_\zeta^{co}}{\partial\zeta_{co}} \\[2mm] \dfrac{1}{R(\zeta_{co})}\dfrac{\partial\Psi_\theta^{co}}{\partial\theta} + \dfrac{\sin(\Theta)}{R(\zeta_{co})}\Psi_\zeta^{co} \\[2mm] \dfrac{\partial\Psi_\theta^{co}}{\partial\zeta_{co}} + \dfrac{1}{R(\zeta_{co})}\dfrac{\partial\Psi_\zeta^{co}}{\partial\theta} - \dfrac{\sin(\Theta)}{R(\zeta_{co})}\Psi_\theta^{co} \\[2mm] 0 \\[2mm] 0 \end{Bmatrix}. \quad (45)$$

The curvatures and mid-surface displacements relation related to the hemispherical part is formulated as the following expressions:

$$\begin{Bmatrix} \chi_\zeta^{hs} \\ \chi_\theta^{hs} \\ \chi_{\zeta\theta}^{hs} \\ \chi_{\zeta\eta}^{hs} \\ \chi_{\theta\eta}^{hs} \end{Bmatrix} = \begin{Bmatrix} \dfrac{1}{R}\dfrac{\partial\Psi_\zeta^{hs}}{\partial\zeta_{hs}} \\[2mm] \dfrac{1}{R\sin(\zeta_{hs})}\dfrac{\partial\Psi_\theta^{hs}}{\partial\theta} + \dfrac{\cot(\zeta_{hs})}{R}\Psi_\zeta^{hs} \\[2mm] \dfrac{1}{R}\dfrac{\partial\Psi_\theta^{hs}}{\partial\zeta_{hs}} + \dfrac{1}{R\sin(\zeta_{hs})}\dfrac{\partial\Psi_\zeta^{hs}}{\partial\theta} - \dfrac{\cot(\zeta_{hs})}{R}\Psi_\theta^{hs} \\[2mm] 0 \\[2mm] 0 \end{Bmatrix}. \quad (46)$$

The stress–strain relation of the joined hemispherical–cylindrical–conical shell can be obtained employing Hook's law as follows:

$$\begin{bmatrix} \sigma_\zeta^i \\ \sigma_\theta^i \\ \tau_{\zeta\theta}^i \\ \tau_{\zeta\eta}^i \\ \tau_{\theta\eta}^i \end{bmatrix} = \begin{bmatrix} C_{11}(\eta) & C_{12}(\eta) & 0 & 0 & 0 \\ C_{12}(\eta) & C_{22}(\eta) & 0 & 0 & 0 \\ 0 & 0 & C_{44}(\eta) & 0 & 0 \\ 0 & 0 & 0 & C_{55}(\eta) & 0 \\ 0 & 0 & 0 & 0 & C_{66}(\eta) \end{bmatrix} \begin{bmatrix} \varepsilon_\zeta^i \\ \varepsilon_\theta^i \\ \gamma_{\zeta\theta}^i \\ \gamma_{\zeta\eta}^i \\ \gamma_{\theta\eta}^i \end{bmatrix}, \quad (47)$$

where the C_{ij} is the coefficient of HM nanocomposite porous hybrid three-phase material. Due to the porosity of HM throughout the thickness of the hemispherical–cylindrical–conical shell, these parameters are written in the terms of η as follows:

$$C_{11}(\eta) = \frac{E_1^{eff}(\eta)}{1-\nu_{12}^{eff}(\eta)\nu_{21}^{eff}(\eta)}, \quad C_{22}(\eta) = \frac{E_2^{eff}(\eta)}{1-\nu_{12}^{eff}(\eta)\nu_{21}^{eff}(\eta)}, \quad C_{12}(\eta) = \frac{\nu_{12}^{eff}(\eta)E_1^{eff}(\eta)}{1-\nu_{12}^{eff}(\eta)\nu_{21}^{eff}(\eta)},$$
$$C_{44}(\eta) = G_{23}^{eff}(\eta), \qquad C_{55}(\eta) = G_{13}^{eff}(\eta), \qquad C_{66}(\eta) = G_{12}^{eff}(\eta)$$
$$(48)$$

The force and moment resultants of each part of the hemispherical–cylindrical–conical shell can be obtained applying the stresses integration along with the thickness of the shell as follows:

$$\begin{bmatrix} N_\zeta^i \\ N_\theta^i \\ N_{\zeta\theta}^i \end{bmatrix} = \int_{-\frac{h}{2}}^{\frac{h}{2}} \begin{bmatrix} \sigma_\zeta^i \\ \sigma_\theta^i \\ \tau_{\zeta\theta}^i \end{bmatrix} d\eta, \quad \begin{bmatrix} M_\zeta^i \\ M_\theta^i \\ M_{\zeta\theta}^i \end{bmatrix} = \int_{-\frac{h}{2}}^{\frac{h}{2}} \eta \cdot \begin{bmatrix} \sigma_\zeta^i \\ \sigma_\theta^i \\ \tau_{\zeta\theta}^i \end{bmatrix} d\eta,$$

$$\begin{bmatrix} Q_{\zeta\eta}^i \\ Q_{\theta\eta}^i \end{bmatrix} = \int_{-\frac{h}{2}}^{\frac{h}{2}} \kappa \begin{bmatrix} \sigma_{\zeta\eta}^i \\ \sigma_{\theta\eta}^i \end{bmatrix} d\eta \quad \text{for } i = \text{co,cy,hs}$$
$$(49)$$

where N_ζ^i, N_θ^i are the resultant axial forces while $N_{\zeta\theta}^i$ stands for the resultant shear force. $Q_{\zeta\eta}^i$, $Q_{\theta\eta}^i$ define the resultant transversely shear forces of joined hemispherical–cylindrical–conical shell. The resultant moment and torsion are shown via M_ζ^i, M_θ^i and $M_{\zeta\theta}^i$, respectively. The resultants of force and moment of the joined hemispherical–cylindrical–conical shell can be formulated in terms of mid-surface strains using a transformation matrix. Substituting Eqs. (40) and (47) into Eq. (49), the following expression is found for each part of the shell:

$$\begin{bmatrix} N_\zeta^i \\ N_\theta^i \\ N_{\zeta\theta}^i \\ M_\zeta^i \\ M_\theta^i \\ M_{\zeta\theta}^i \\ Q_{\zeta\eta}^i \\ Q_{\theta\eta}^i \end{bmatrix} = \begin{bmatrix} A_{11} & A_{12} & 0 & \bar{A}_{11} & \bar{A}_{12} & 0 & 0 & 0 \\ A_{12} & A_{22} & 0 & \bar{A}_{12} & \bar{A}_{22} & 0 & 0 & 0 \\ 0 & 0 & A_{66} & 0 & 0 & \bar{A}_{66} & 0 & 0 \\ \bar{A}_{11} & \bar{A}_{12} & 0 & \bar{\bar{A}}_{11} & \bar{\bar{A}}_{12} & 0 & 0 & 0 \\ \bar{A}_{12} & \bar{A}_{22} & 0 & \bar{\bar{A}}_{12} & \bar{\bar{A}}_{22} & 0 & 0 & 0 \\ 0 & 0 & \bar{A}_{66} & 0 & 0 & \bar{\bar{A}}_{66} & 0 & 0 \\ 0 & 0 & 0 & 0 & 0 & 0 & \kappa A_{44} & 0 \\ 0 & 0 & 0 & 0 & 0 & 0 & 0 & \kappa A_{55} \end{bmatrix} \begin{bmatrix} \bar{\varepsilon}_\zeta^i \\ \bar{\varepsilon}_\theta^i \\ \bar{\gamma}_{\zeta\theta}^i \\ \chi_\zeta^i \\ \chi_\theta^i \\ \chi_{\zeta\theta}^i \\ \bar{\gamma}_{\theta\eta}^i \\ \bar{\gamma}_{\zeta\eta}^i \end{bmatrix} \quad \text{for } i = \text{co,cy,hs.} \quad (50)$$

In this work, the shear factor κ is assumed to be $\frac{5}{6}$, and the stiffness factors $\left(A_{ij}, \bar{A}_{ij}, \bar{\bar{A}}_{ij}\right)$ are expressed as follows:

$$\begin{bmatrix} A_{ij} \\ \bar{A}_{ij} \\ \bar{\bar{A}}_{ij} \end{bmatrix} = \int_{-\frac{h}{2}}^{\frac{h}{2}} \begin{bmatrix} C_{ij}(\eta) \\ \eta C_{ij}(\eta) \\ \eta^2 C_{ij}(\eta) \end{bmatrix} d\eta \qquad i,j = 1,2,4,5,6. \quad (51)$$

5 The equations of motion

The joined hemispherical–cylindrical–conical shell-governing equations of motion are derived by employing Hamilton's principle and Donnell's approach in this research [99]. The basic formulation of this principle is given by

$$\delta \int_{t_1}^{t_2} [K_i - (V_i + \Pi_i)]dt = 0 \quad (52)$$

for $\quad$ i = co,cy,sh,

where δK_i defines the kinetic energy and can be expressed for each part of joined hemispherical–cylindrical–conical shell as follows:

$$\delta K_i = \int_{V_i} \rho_{eff}^{(I,II,III)}(\eta)(\dot{U}_1^i \, \delta \, \dot{U}_1^i + \dot{U}_2^i \, \delta \, \dot{U}_2^i + \dot{U}_3^i \, \delta \, \dot{U}_3^i)dV_i \quad (53)$$

for $\quad$ i = co,cy,sh,

where (˙) indicates the derivative with respect to time.

In addition, $\delta\Pi_i$ is the strain energy of each segment of the structure and expressed as follows:

$$\delta\Pi_i = \int_{A_i} \int_{-\frac{h}{2}}^{\frac{h}{2}} [\sigma_\zeta^i \delta\varepsilon_\zeta^i + \sigma_\theta^i \delta\varepsilon_\theta^i + \tau_{\zeta\theta}^i \delta\gamma_{\zeta\theta}^i + \kappa\tau_{\zeta\eta}^i \delta\gamma_{\zeta\eta}^i + \kappa\tau_{\theta\eta}^i \delta\gamma_{\theta\eta}^i] \, d\eta dA_i$$

for $\quad$ i = co,cy,hs.
$$(54)$$

Based on Hamilton's principle the following statements can be expressed as follows:

at $\quad t = t_1, t_2: \quad \delta u_1^i = \delta u_2^i = \delta u_3^i = \delta\Psi_\zeta^i = \delta\Psi_\theta^i$

for $\quad$ i = co,cy,hs.
$$(55)$$

Moreover, using Eqs. (50), (52)–(54), performing the integration along the thickness direction, and employing Green-Gauss theory, the governing differential equations

of motion of cylindrical segment of the joined hemispherical–cylindrical–conical shell is found as follows:

$$\delta u_1^{cy} : \frac{\partial N_\zeta^{cy}}{\partial \zeta_{cy}} + \frac{\partial N_{\zeta\theta}^{cy}}{\partial \theta} \frac{1}{R} = I_1 \ddot{u}_1^{cy} + I_2 \ddot{\Psi}_\zeta^{cy}$$

$$\delta u_2^{cy} : \frac{\partial N_\theta^{cy}}{\partial \theta} \frac{1}{R} + \frac{\partial N_{\zeta\theta}^{cy}}{\partial \zeta_{cy}} + \frac{Q_{\theta\eta}^{cy}}{R} = I_1 \ddot{u}_2^{cy} + I_2 \ddot{\Psi}_\theta^{cy}$$

$$\delta u_3^{cy} : \frac{\partial Q_{\zeta\eta}^{cy}}{\partial \zeta_{cy}} + \frac{1}{R} \frac{\partial Q_{\theta\eta}^{cy}}{\partial \theta} - \frac{N_\theta^{cy}}{R} = I_1 \ddot{u}_3^{cy} \qquad (56)$$

$$\delta \Psi_\zeta^{cy} : \frac{\partial M_\zeta^{cy}}{\partial \zeta_{cy}} + \frac{\partial M_{\zeta\theta}^{cy}}{\partial \theta} \frac{1}{R} - Q_{\zeta\eta}^{cy} = I_2 \ddot{u}_1^{cy} + I_3 \ddot{\Psi}_\zeta^{cy}$$

$$\delta \Psi_\theta^{cy} : \frac{\partial M_{\zeta\theta}^{cy}}{\partial \zeta_{cy}} + \frac{\partial M_\theta^{cy}}{\partial \theta} \frac{1}{R} - Q_{\theta\eta}^{cy} = I_2 \ddot{u}_2^{cy} + I_3 \ddot{\Psi}_\theta^{cy}.$$

Furthermore, the governing differential equations of motion for the conical part of joined hemispherical–cylindrical–conical shell can be found using the same above-mentioned procedure as follows:

$$\delta u_1^{co} : \frac{\partial N_\zeta^{co}}{\partial \zeta_{co}} + \frac{\partial N_{\zeta\theta}^{co}}{\partial \theta} \frac{1}{R(\zeta_{co})} + \frac{\sin(\Theta)}{R(\zeta_{co})}(N_\zeta^{co} - N_\theta^{co}) = I_1 \ddot{u}_1^{co} + I_2 \ddot{\Psi}_\zeta^{co}$$

$$\delta u_2^{co} : \frac{\partial N_\theta^{co}}{\partial \theta} \frac{1}{R(\zeta_{co})} + \frac{\partial N_{\zeta\theta}^{co}}{\partial \zeta_{co}} + 2\frac{\sin(\Theta)}{R(\zeta_{co})}N_{\zeta\theta}^{co} + \frac{\cos(\Theta)}{R(\zeta_{co})}Q_{\theta\eta}^{co} = I_1 \ddot{u}_2^{co} + I_2 \ddot{\Psi}_\theta^{co}$$

$$\delta u_3^{co} : \frac{\partial Q_{\zeta\eta}^{co}}{\partial \zeta_{co}} + \frac{1}{R(\zeta_{co})} \frac{\partial Q_{\theta\eta}^{co}}{\partial \theta} + \frac{\sin(\Theta)}{R(\zeta_{co})}Q_{\zeta\eta}^{co} - \frac{\cos(\Theta)}{R(\zeta_{co})}N_\theta^{co} = I_1 \ddot{u}_3^{co} \qquad (57)$$

$$\delta \Psi_\zeta^{co} : \frac{\partial M_\zeta^{co}}{\partial \zeta_{co}} + \frac{\partial M_{\zeta\theta}^{co}}{\partial \theta} \frac{1}{R(\zeta_{co})} + \frac{\sin(\Theta)}{R(\zeta_{co})}(M_\zeta^{co} - M_\theta^{co}) - Q_{\zeta\eta}^{co} = I_2 \ddot{u}_1^{co} + I_3 \ddot{\Psi}_\zeta^{co}$$

$$\delta \Psi_\theta^{co} : \frac{\partial M_{\zeta\theta}^{co}}{\partial \zeta_{co}} + \frac{\partial M_\theta^{co}}{\partial \theta} \frac{1}{R(\zeta_{co})} + 2\frac{\sin(\Theta)}{R(\zeta_{co})}M_{\zeta\theta}^{co} - Q_{\theta\eta}^{co} = I_2 \ddot{u}_2^{co} + I_3 \ddot{\Psi}_\theta^{co}.$$

On the other hand, the governing equations of motion associated to the hemispherical part of the shell can be obtained utilizing the similar mathematical operation concerning the others segment of joined hemispherical–cylindrical–conical shell as follows:

$$\delta u_1^{hs} : \frac{1}{R} \frac{\partial N_\zeta^{hs}}{\partial \zeta_{hs}} + \frac{\partial N_{\zeta\theta}^{hs}}{\partial \theta} \frac{1}{R\sin(\zeta_{hs})} + \frac{\cot(\zeta_{hs})}{R}(N_\zeta^{hs} - N_\theta^{hs}) + \frac{Q_{\zeta\eta}^{hs}}{R} = I_1 \ddot{u}_1^{hs} + I_2 \ddot{\Psi}_\zeta^{hs}$$

$$\delta u_2^{hs} : \frac{\partial N_\theta^{hs}}{\partial \theta} \frac{1}{R\sin(\zeta_{hs})} + \frac{\partial N_{\zeta\theta}^{hs}}{\partial \zeta_{hs}} + 2\frac{\cot(\zeta_{hs})}{R}N_{\zeta\theta}^{hs} + \frac{Q_{\theta\eta}^{hs}}{R} = I_1 \ddot{u}_2^{hs} + I_2 \ddot{\Psi}_\theta^{hs}$$

$$\delta u_3^{hs} : \frac{1}{R} \frac{\partial Q_{\zeta\eta}^{hs}}{\partial \zeta_{hs}} + \frac{1}{R\sin(\zeta_{hs})} \frac{\partial Q_{\theta\eta}^{hs}}{\partial \theta} + \frac{\cot(\zeta_{hs})}{R}Q_{\zeta\eta}^{hs} - \frac{(N_\theta^{hs} + N_\zeta^{hs})}{R} = I_1 \ddot{u}_3^{hs} \qquad (58)$$

$$\delta \Psi_\zeta^{hs} : \frac{1}{R} \frac{\partial M_\zeta^{hs}}{\partial \zeta_{hs}} + \frac{\partial M_{\zeta\theta}^{hs}}{\partial \theta} \frac{1}{R\sin(\zeta_{hs})} + \frac{\cot(\zeta_{hs})}{R}(M_\zeta^{hs} - M_\theta^{hs}) - Q_{\zeta\eta}^{hs} = I_2 \ddot{u}_1^{hs} + I_3 \ddot{\Psi}_\zeta^{hs}$$

$$\delta \Psi_\theta^{hs} : \frac{1}{R} \frac{\partial M_{\zeta\theta}^{hs}}{\partial \zeta_{hs}} + \frac{\partial M_\theta^{hs}}{\partial \theta} \frac{1}{R\sin(\zeta_{hs})} + 2\frac{\cot(\zeta_{hs})}{R}M_{\zeta\theta}^{hs} - Q_{\theta\eta}^{hs} = I_2 \ddot{u}_2^{hs} + I_3 \ddot{\Psi}_\theta^{hs}.$$

It should be noted that the inertia coefficients (I_i) of the structure can be found as follows:

$$\begin{bmatrix} I_1 \\ I_2 \\ I_3 \end{bmatrix} = \int_{-\frac{h}{2}}^{\frac{h}{2}} \rho_{eff}^{(I,II,III)}(\eta) \begin{bmatrix} 1 \\ \eta \\ \eta^2 \end{bmatrix} d\eta. \qquad (59)$$

5.1 The boundary conditions

According to the type of structures in this study, the boundary conditions are differentiated by various forms. Based on this issue, joined shells are assumed to be restrained with Clamped (C), Simply supported (S), and Free (F) ends. The mathematical expressions of these boundary conditions for the ends of the joined hemispherical–cylindrical–conical shell structure are given as follows:

$$F_{hs} : N_\zeta^{hs} = N_{\zeta\theta}^{hs} = Q_{\zeta\eta}^{hs} = M_\zeta^{hs} = M_{\zeta\theta}^{hs} = 0$$
$$S_{hs} : u_1^{hs} = u_2^{hs} = u_3^{hs} = M_\zeta^{hs} = \Psi_\theta^{hs} = 0$$
$$C_{hs} : u_1^{hs} = u_2^{hs} = u_3^{hs} = \Psi_\zeta^{hs} = \Psi_\theta^{hs} = 0$$
$$F_{co} : N_\zeta^{co} = N_{\zeta\theta}^{co} = Q_{\zeta\eta}^{co} = M_\zeta^{co} = M_{\zeta\theta}^{co} = 0 \quad (60)$$
$$S_{co} : u_1^{co} = u_2^{co} = u_3^{co} = M_\zeta^{co} = \Psi_\theta^{co} = 0$$
$$C_{co} : u_1^{co} = u_2^{co} = u_3^{co} = \Psi_\zeta^{co} = \Psi_\theta^{co} = 0.$$

5.2 Coupling conditions

The coupling conditions of joined hemispherical–cylindrical–conical shells can be found for each part including hemispherical–cylindrical and cylindrical–conical parts. Note that these conditions are considered, separately.

First, the displacement conditions at the connection of hemispherical–cylindrical shells are given as follows:

$$u_1^{hs} = u_1^{cy}$$
$$u_2^{hs} = u_2^{cy}$$
$$u_3^{hs} = u_3^{cy} \quad (61)$$
$$\Psi_\zeta^{hs} = \Psi_\zeta^{cy}$$
$$\Psi_\theta^{hs} = \Psi_\theta^{cy}.$$

$$\begin{Bmatrix} u_1^i(\zeta_i,\theta,t) \\ u_2^i(\zeta_i,\theta,t) \\ u_2^i(\zeta_i,\theta,t) \\ \Psi_\zeta^i(\zeta_i,\theta,t) \\ \Psi_\theta^i(\zeta_i,\theta,t) \end{Bmatrix} = \cos(\omega_n t) \begin{bmatrix} \sin(n\theta) & 0 & 0 & 0 & 0 \\ 0 & \cos(n\theta) & 0 & 0 & 0 \\ 0 & 0 & \sin(n\theta) & 0 & 0 \\ 0 & 0 & 0 & \sin(n\theta) & 0 \\ 0 & 0 & 0 & 0 & \cos(n\theta) \end{bmatrix} \begin{Bmatrix} \bar{U}_1^i(\zeta_i) \\ \bar{U}_2^i(\zeta_i) \\ \bar{U}_3^i(\zeta_i) \\ \bar{\Psi}_\zeta^i(\zeta_i) \\ \bar{\Psi}_\theta^i(\zeta_i) \end{Bmatrix} \quad (65)$$

for i = co,cy,hs,

Then, the conditions used for movement at the connection of cylindrical–conical shells are as follows:

$$u_1^{cy} = u_1^{co}\cos(\Theta) - u_3^{co}\sin(\Theta)$$
$$u_3^{cy} = u_1^{co}\sin(\Theta) + u_3^{co}\cos(\Theta)$$
$$u_2^{cy} = u_2^{co} \quad (62)$$
$$\Psi_\zeta^{cy} = \Psi_\zeta^{co}$$
$$\Psi_\theta^{cy} = \Psi_\theta^{co}.$$

Furthermore, the compatible conditions for resultant forces and moments at the connection of hemispherical–cylindrical can be defined as follows:

$$N_\zeta^{hs} = N_\zeta^{cy}$$
$$Q_{\zeta\eta}^{hs} = Q_{\zeta\eta}^{cy}$$
$$M_\zeta^{hs} = M_\zeta^{cy} \quad (63)$$
$$N_{\zeta\theta}^{hs} = N_{\zeta\theta}^{cy}$$
$$M_{\zeta\theta}^{hs} = M_{\zeta\theta}^{cy}.$$

Moreover, the consistent conditions related to the force and moment resultants at the intersection of cylindrical–conical are accessed by

$$N_\zeta^{cy} = N_\zeta^{co}\cos(\Theta) - Q_{\zeta\eta}^{co}\sin(\Theta)$$
$$Q_{\zeta\eta}^{cy} = N_\zeta^{co}\sin(\Theta) + Q_{\zeta\eta}^{co}\cos(\Theta)$$
$$M_\zeta^{cy} = M_\zeta^{co} \quad (64)$$
$$N_{\zeta\theta}^{cy} = N_{\zeta\theta}^{co}$$
$$M_{\zeta\theta}^{cy} = M_{\zeta\theta}^{co}.$$

The natural frequencies of joined hemispherical–cylindrical–conical shells can be calculated by solving the governing differential equations of motion. Hence, these equations can be obtained by applying the relation between the resultants of force and the moment in terms of mid-surface displacements. In addition, the following expressions are considered for the displacement fields of the structure:

where ω_n, n are the natural frequency and the circumferential wave number of joined shells, respectively.

It should be noted that the governing equations of motion of each part of this joined structure can be transformed concerning the $\bar{U}_1^i(\zeta_i), \bar{U}_2^i(\zeta_i), \bar{U}_3^i(\zeta_i), \bar{\Psi}_\zeta^i(\zeta_i), \bar{\Psi}_\theta^i(\zeta_i)$ functions utilizing Eq. (65). After that, the obtained governing equations only depend on the longitudinal direction, which can be found for each segment of the joined hemispherical–cylindrical–conical shell. Accordingly, the natural frequencies of this structure can be determined by solving 15 equations (5 for hemispherical, 5 for cylindrical, and 5 for conical segments), simultaneously. In addition, the related equations are given in Appendix I.

6 The solution procedure

In this work, the differential equations of motions related to the joined hemispherical–cylindrical–conical shell are solved by applying a qualified semi-analytical solution, namely GDQM. It should also be noted that the GDQM technique is used for derivative equations of motion and implemented boundary and coupled conditions based on using grid points. The GDQM is continued by the Lagrangian polynomials and Chebyshev–Gauss–Lobatto to realize weighting coefficients and grid points distribution pattern, respectively. On this basis, the governing equations of motion associated with the joined hemispherical–cylindrical–conical shell can be written for each grid point as follows:

$$[\mathfrak{R}_{dd}][X_d] + [\mathfrak{R}_{db}][X_b] + [\mathfrak{R}_{dc}][X_c] = \omega_n^2[M_{dd}][X_d], \tag{66}$$

where $[\mathfrak{R}_{dd}]$ and $[\mathfrak{R}_{dd}]$ are interior point stiffness and mass matrices, respectively. The inner stiffness matrix due to stiffness of intersection grids is represented by $[\mathfrak{R}_{dc}]$. In addition, $[X_d]$, $[X_b]$ and $[X_c]$ indicate the displacement vector of the interior, boundary, and connective conditions, respectively. On the other hand, the interior stiffness matrix as a product of the stiffness of boundary points is defined by $[\mathfrak{R}_{db}]$. It should be noticed that five equations are built for each part of joined hemispherical–cylindrical–conical shell structure. Hence, there are 15 equations for the joined hemispherical–cylindrical–conical shell. Furthermore, each grid point should be filled in these 15 equations. In addition, by applying GDQM and considering boundary and coupling conditions, the following equations can be defined:

$$[\mathfrak{R}_{bb}][X_b] + [\mathfrak{R}_{bd}][X_d] + [\mathfrak{R}_{bc}][X_c] = 0 \tag{67}$$

$$[\mathfrak{R}_{cc}][X_c] + [\mathfrak{R}_{cd}][X_d] + [\mathfrak{R}_{cb}][X_b] = 0, \tag{68}$$

where the stiffness matrices of boundary and connective points are represented by $[\mathfrak{R}_{bb}]$ and $[\mathfrak{R}_{cc}]$, respectively.

Moreover, $[\mathfrak{R}_{bd}]$ and $[\mathfrak{R}_{bc}]$ are the boundary stiffness matrices including the stiffness of interior and connection points. The connective stiffness matrices caused by the stiffness of interior and boundary grids are shown with $[\mathfrak{R}_{cd}]$ and $[\mathfrak{R}_{cb}]$, respectively.

Furthermore, there are ten boundary conditions related to the end restrains of the joined hemispherical–cylindrical–conical shell, as well as 20 connection conditions are also employed for the structure. Note that there are several methods to include the boundary and connection conditions in the differential equations of motion.

The governing equations of interior points can be obtained by substituting relations (67) and (68) into (66). Therefore, the natural frequencies of joined hemispherical–cylindrical–conical shells are obtained applying the eigenvalue of the linear governing equations of motion as follows:

$$\left| \mathfrak{R}^{eff} - \omega_n M^{eff} \right| = 0 \tag{69}$$

in which

$$
\begin{aligned}
[\mathfrak{R}^{eff}] =\, & [\mathfrak{R}_{dd}] + \{[\mathfrak{R}_{db}]([\mathfrak{R}_{bb}] \\
& - [\mathfrak{R}_{bc}][\mathfrak{R}_{cc}]^{-1}[\mathfrak{R}_{cb}])^{-1}([\mathfrak{R}_{bd}] \\
& - [\mathfrak{R}_{bc}][\mathfrak{R}_{cc}]^{-1}[\mathfrak{R}_{cd}])\} \\
& + [[\mathfrak{R}_{dc}](-([\mathfrak{R}_{cc}]^{-1})([\mathfrak{R}_{cd}] + \{[\mathfrak{R}_{cb}]([\mathfrak{R}_{bb}] \\
& - [\mathfrak{R}_{bc}][\mathfrak{R}_{cc}]^{-1}[\mathfrak{R}_{cb}])^{-1} \\
& ([\mathfrak{R}_{bd}] - [\mathfrak{R}_{bc}][\mathfrak{R}_{cc}]^{-1}[\mathfrak{R}_{cd}])\}))] \\
& [M^{eff}] = [M_{dd}].
\end{aligned}
\tag{70}
$$

Finally, the dimension of the effective stiffness matrix is $15N - 30$. In addition, N stands for the number of total grids. Accordingly, there are 15 grids are employed to the discretization of the shell structures [100]. Afterward, the dimension of the effective stiffness matrix is found as 195-by-195.

7 Results and discussion

At first, some comparison studies are performed with the available results of open literature to verify the proposed formulation. Then, some new, applicable, and complicated problems associated with nonhomogeneous and homogenous joined hemispherical–cylindrical–conical shells are solved numerically to show the high accuracy and capability of the proposed formulation. The effects of different boundary conditions, material properties, and geometrical characteristics on the vibrational behavior of joined shells are also discussed. Here, F, S, and C represent the free, simply supported, and clamped boundary conditions, respectively.

7.1 Verification study

This example deals to verify the proposed formulation and solution method comparing the natural frequency of the hemispherical–cylindrical–conical structure having the following geometrical and material properties with the results of [66, 68]. The boundary condition of the shell is supposed to be F–F:

$R=1, \quad L_{cy}=2.5, \quad R_{co}^1=0.4, \quad h=0.01, \quad \Theta=-\frac{\pi}{6}, \quad \vartheta=\left\{0, \frac{\pi}{6}, \frac{\pi}{4}\right\}$

$E = 69.58\,(\text{GPa}), \quad \nu = 0.31, \quad \rho = 2700\,(\text{kgm}^{-3}).$

Table 4 The natural frequencies of isotropic joined hemispherical–cylindrical–conical shells under F–F boundary conditions

n	m	$\vartheta = 0$			$\vartheta = 30°$			$\vartheta = 45°$		
		Present	Ref. [68]	Ref. [66]	Present	Ref. [68]	Ref. [66]	Present	Ref. [68]	Ref. [66]
0	1	423.92	423.92	423.92	426.25	426.26	426.25	434.04	434.04	434.04
	2	430.56	428.80	429.13	438.93	437.65	438.53	447.24	447.38	446.88
	3	601.50	601.85	601.59	634.31	633.68	634.38	669.76	670.08	669.80
	4	731.46	731.56	731.50	753.84	753.71	753.88	766.18	766.22	766.22
	5	766.82	766.73	766.86	782.30	782.22	782.40	794.61	794.72	794.72
	6	787.24	787.42	787.34	798.36	798.42	798.45	801.01	801.10	801.13
1	1	353.86	353.31	353.46	365.75	364.76	365.36	380.10	379.28	379.71
	2	490.12	490.28	490.13	492.07	492.01	492.07	495.87	495.93	495.88
	3	585.52	585.62	585.60	593.75	593.75	593.93	602.40	602.42	602.61
	4	629.18	629.45	629.20	636.90	636.73	636.91	646.55	646.56	646.57
	5	701.01	700.99	700.93	714.83	714.86	714.86	724.34	724.36	724.38
	6	723.21	723.24	723.24	728.62	728.66	728.66	746.62	746.68	746.69
2	1	24.46	24.14	24.41	23.98	23.72	23.97	13.96	13.97	14.05
	2	143.08	142.53	142.92	32.81	32.85	33.06	25.44	25.05	25.35
	3	345.29	345.25	345.27	160.95	160.67	160.79	176.26	176.04	176.05
	4	489.09	489.43	489.16	359.72	359.77	359.71	373.64	373.71	373.65
	5	570.67	570.62	570.69	497.80	497.80	497.86	505.37	505.78	505.42
	6	645.99	646.03	646.03	578.32	578.26	578.34	584.66	584.63	584.69
3	1	67.64	67.41	67.69	67.46	67.39	67.51	47.53	47.68	47.78
	2	92.08	91.95	92.03	89.43	89.43	89.54	69.52	69.42	69.57
	3	250.07	250.09	250.08	108.77	109.38	109.58	99.67	99.55	99.63
	4	366.13	366.12	366.15	251.52	251.48	251.53	256.32	256.15	256.34
	5	436.81	436.77	436.86	366.62	366.07	366.63	368.29	368.17	368.30
	6	543.24	543.27	543.33	437.69	437.65	437.74	440.72	440.67	440.77

The results are reported in Table 4. It is seen that there is a good agreement between the results of the present study and the results of the references.

7.2 Convergence study

In this example, the results of the natural frequency of the joined hemispherical–cylindrical–conical shells are compared with the results of the structure modeled in a commercial FEM software called ABAQUS. This analysis is performed under the C–F boundary conditions. The results related to the first mode of the circumferential wave number of 0, 1, 2, 3, and 4 are reported. The material and geometric properties of the structure are the same as in the earlier example, as well as two different values of thickness including 0.02 and 0.05 are considered.

Table 5 reports the natural frequency of the homogenous joined hemispherical–cylindrical–conical shells under C–F boundary conditions. In addition, the mode shapes of the joined shells with thickness value 0.02 are also illustrated in Fig. 7.

7.3 The effect of different patterns of porosity distribution

The main goal of this example is to study the effect of three different patterns of porosity distribution on the natural frequencies of joined hemispherical–cylindrical–conical shells. Different types of boundary conditions are considered in this part. The volume fraction of fibers is assumed to equal 0.6. The results associated with the first mode of the first ten circumferential waves are obtained. The geometric characteristics of the shell are as follows: $R=1, \ L_{cy}=2.5, \ L_{co}=1, \ h=0.01, \ \Theta=-\frac{\pi}{6}, \ \vartheta=\frac{\pi}{6}$.

In the first part, the responses related to the boundary condition of C–C are presented for different porosity patterns. Table 6 reports the natural frequency of the joined

shells constructed with hybrid matrix nanocomposite shells including porosity with different patterns of distribution.

It is seen that the natural frequencies of the joined shell decrease with the increasing porosity factor in all patterns. In the second part, different boundary conditions are considered for the structure with the porosity factor of 0.6. Figure 8 depicts the variation of the natural frequency of the structure with different boundary conditions.

The lowest values of the natural frequency of the joined shell are obtained under C–C boundary conditions for the first pattern of porosity distribution in the fifth circumferential wave number, while for the sixth circumferential wave in the second and third patterns of porosity distribution. Furthermore, for the boundary conditions of C–F and F–C, the lowest frequency of the joined shell is reported for the second circumferential wave number for all patterns of porosity distribution. This parameter is minimized at the first circumferential wave as the boundary condition of the structure is S–F, F–S, or F–F for all patterns of porosity distribution.

## 7.4 The effect of the meridional angle of the hemispherical part

This example studies the effect of the meridional angle of the hemispherical part of the joined shell on the natural frequency of the hybrid porous nanocomposite joined hemispherical–cylindrical–conical shells having the first pattern of the porosity distribution with the porosity factor of 0.1, as well as the volume fraction of the AS4 carbon fibers is equal to 0.6. The geometric properties of the joined shell are considered as follows: $R=1, \ L_{cy}=2.5, \ L_{co}=1, \ \Theta=-\frac{\pi}{6}$.

At first, the thickness of the structure is assumed to be 0.01 and different boundary conditions are considered. The results are found for the first mode of the first circumferential wave number and presented in Table 7.

Then, different values of thickness including 0.01, 0.02, 0.05, and 0.1 are considered for the C–C joined

Table 5 The natural frequencies of isotropic joined hemispherical–cylindrical–conical shells under C–F boundary conditions

h	n	Number of grid points (N)								ABAQUS
		5	7	9	11	13	15	17	19	
0.02	0	149.2510	146.5910	150.1825	150.1915	150.1936	150.1952	150.1952	150.1952	150.2700
	1	26.0189	19.5530	25.1607	26.5698	26.6282	26.6324	26.6324	26.6324	26.6930
	2	27.6226	45.1841	47.1832	47.8028	47.8704	47.8260	47.8260	47.8260	47.4240
	3	96.6369	93.2448	92.0755	91.6087	91.4263	91.3860	91.3860	91.3860	91.6060
	4	97.6731	95.9892	95.2559	95.0182	94.9391	94.9200	94.9200	94.9200	95.9410
0.05	1	149.2690	150.1226	150.2108	150.2249	150.2313	150.2360	150.2360	150.2360	150.3200
	2	26.9295	26.9295	29.2559	29.4758	29.5121	29.5200	29.5200	29.5200	29.4640
	3	99.3470	103.2937	103.9622	104.1100	104.1286	104.1500	104.1500	104.1500	103.7300
	4	136.0406	134.2425	133.6113	133.4485	133.4314	133.4300	133.4300	133.4300	133.7300
	5	200.3998	199.4272	199.0741	198.9967	198.9872	198.9100	198.9100	198.9100	199.8400

(a)

(c)

(b)

(d)

(e)
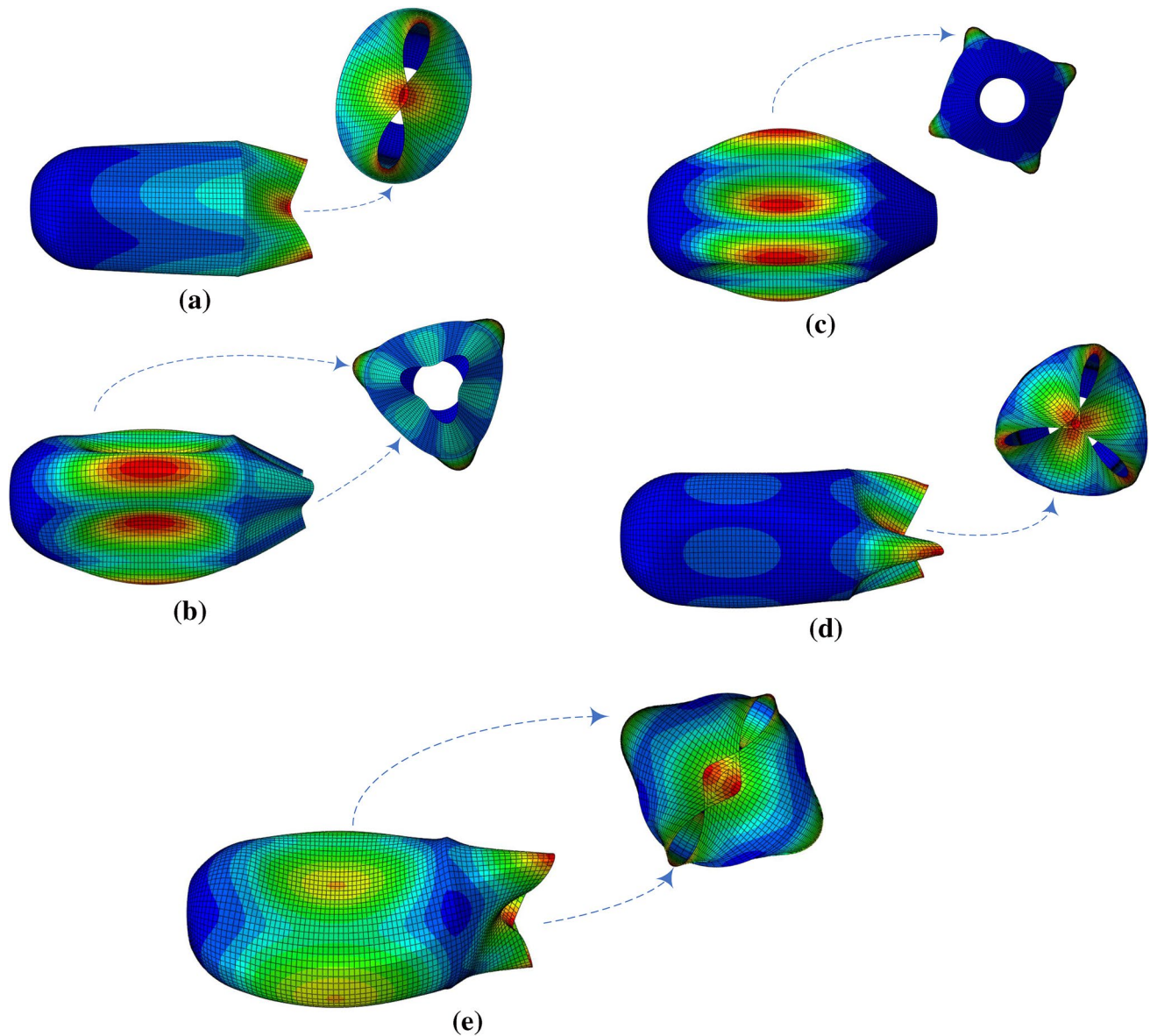
Fig. 7 The variation of mode shapes of the joined isotropic hemispherical–cylindrical–conical shell under C–F boundary conditions (**a**) occurred in the second wave number (47.424 Hz), (**b**) occurred in the third wave number (91.606 Hz), (**c**) occurred in the fourth wave number (95.941 Hz), (**d**) occurred in the second mode of third wave number (142.99 Hz), (**e**) occurred in the second mode of the second wave number (147.41 Hz)

hemispherical–cylindrical–conical shell. The results associated with the first mode of the first five circumferential waves are illustrated in Fig. 9.

It is seen that for all values of the shell thickness, increasing the values of meridional angle of the hemispherical part increases the natural frequency of the structure. Moreover, the lowest frequency of the structure having the thickness of 0.01, 0.02, 0.05, and 0.1 is found for the fifth, fourth, third, and first circumferential waves, respectively.

7.5 The effect of shell thickness

This example investigates the effect of thickness variation on the natural frequencies of the hybrid porous nanocomposite joined hemispherical–cylindrical–conical shells. In this example, the first pattern of the porosity distribution with the coefficient of 0.1 is employed, the volume fraction of AS4 carbon fibers is also supposed to be 0.6, and the following geometric characteristics are considered: $R=1$, $L_{cy}=2.5$, $L_{co}=1$, $\Theta=-\frac{\pi}{6}$, $\vartheta=\frac{\pi}{6}$.
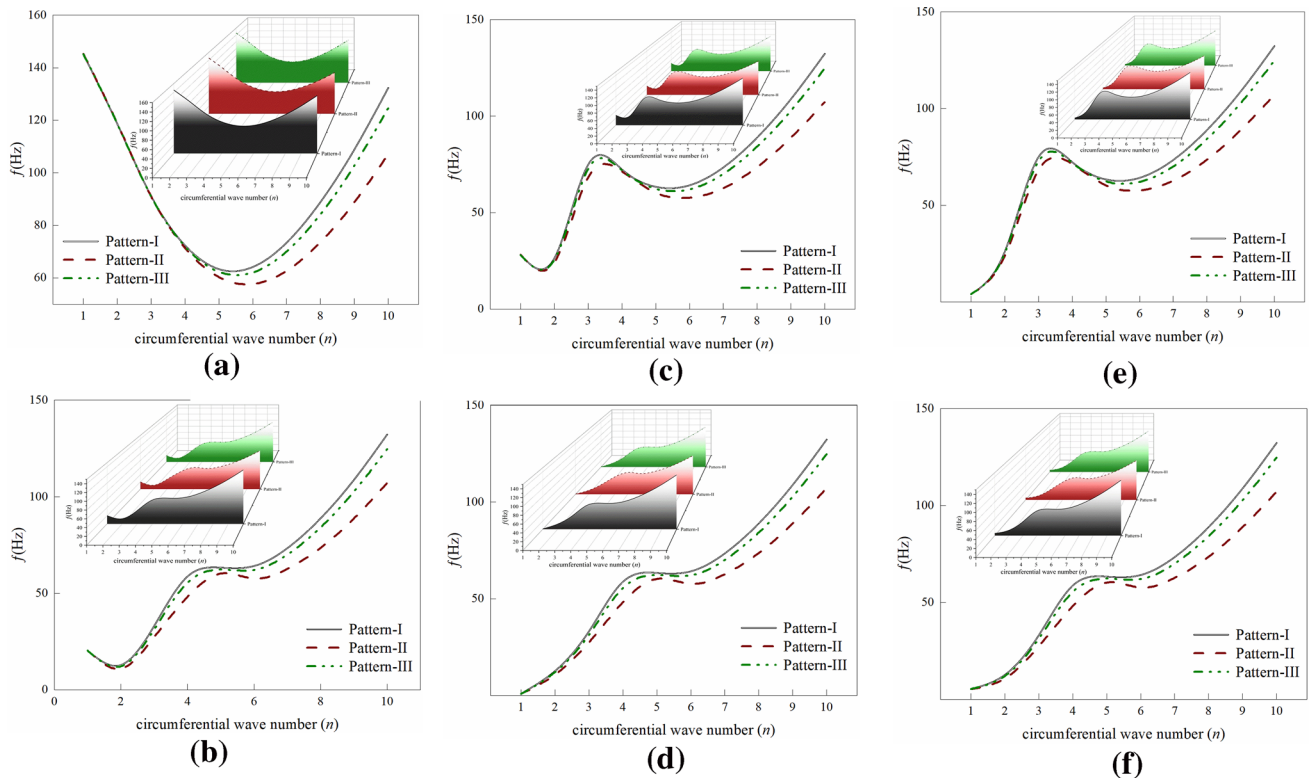
Table 6 The natural frequencies of the first ten wave numbers of hybrid porous nanocomposite joined hemispherical–cylindrical–conical shell versus various porosity patterns

	n	ξ_I						
		0.1	0.2	0.3	0.4	0.5	0.6	0.65
Pattern-I	1	157.8239	155.8979	153.7298	151.2635	148.4231	145.1033	143.2190
	2	128.0489	126.6601	125.0819	123.2689	121.1592	118.6673	117.2416
	3	97.5455	96.6231	95.5662	94.3417	92.9050	91.1939	90.2091
	4	76.4020	75.8290	75.1672	74.3943	73.4796	72.3808	71.7443
	5	65.9456	65.5756	65.1490	64.6516	64.0636	63.3579	62.9494
	6	66.1468	65.8475	65.5100	65.1252	64.6809	64.1604	63.8648
	7	75.4393	75.1157	74.7602	74.3661	73.9249	73.4257	73.1500
	8	91.3148	90.9151	90.4819	90.0090	89.4890	88.9128	88.6004
	9	111.8682	111.3661	110.8245	110.2368	109.5952	108.8903	108.5110
	10	136.0680	135.4469	134.7781	134.0538	133.2650	132.4010	131.9374
	n	ξ_{II}						
		0.1734	0.3426	0.5065	0.6637	0.8112	0.9432	0.9976
Pattern-II	1	157.8057	155.8487	153.6397	151.1341	148.3151	145.2777	143.8815
	2	128.0307	126.6139	125.0005	123.1546	121.0617	118.7951	117.7543
	3	97.5086	96.5391	95.4262	94.1435	92.6804	91.0913	90.3638
	4	76.2834	75.5696	74.7409	73.7730	72.6513	71.4098	70.8320
	5	65.6255	64.8794	64.0052	62.9684	61.7385	60.3271	59.6408
	6	65.4951	64.4286	63.1720	61.6651	59.8427	57.6842	56.5914
	7	74.3893	72.8245	70.9727	68.7353	65.9955	62.6847	60.9678
	8	89.8442	87.7011	85.1577	82.0710	78.2648	73.6142	71.1720
	9	109.9557	107.1823	103.8860	99.8760	94.9136	88.8160	85.5938
	10	133.6824	130.2259	126.1141	121.1057	114.8960	107.2437	103.1870
	n	ξ_{III}						
		0.936	0.8713	0.8058	0.7391	0.6711	0.6012	0.5653
Pattern-III	1	157.8218	155.9008	153.7475	151.2987	148.4816	145.1715	143.2750
	2	128.0455	126.6581	125.0878	123.2837	121.1854	118.6906	117.2478
	3	97.5342	96.6020	95.5375	94.3029	92.8529	91.1108	90.0951
	4	76.3606	75.7423	75.0306	74.1982	73.2113	72.0135	71.3094
	5	65.8316	65.3334	64.7614	64.0933	63.3020	62.3418	61.7770
	6	65.9143	65.3523	64.7149	63.9800	63.1206	62.0913	61.4918
	7	75.0649	74.3175	73.4770	72.5166	71.4045	70.0864	69.3252
	8	90.7907	89.7971	88.6833	87.4151	85.9521	84.2256	83.2320
	9	111.1869	109.9120	108.4844	106.8606	104.9897	102.7848	101.5174
	10	135.2183	133.6332	131.8586	129.8407	127.5167	124.7788	123.2055

At first, all types of boundary conditions are studied, and results of natural frequency related to the first circumferential wave number of the first mode are given in Table 8.

Then, the results of the natural frequency of the hemispherical–cylindrical–conical shells associated with the first five circumferential waves of the first mode are obtained for the boundary conditions of C–C, C–F, F–C, and F–S and illustrated in Fig. 10.

It is noticed that in all cases, increasing the thickness of the structure increases the natural frequency of the shell. In addition, in the case of the C–C boundary conditions, increasing the thickness of the structure causes that the lowest natural frequency of shell is obtained for the different number of circumferential waves. On the other hand, in the cases of C–F and F–C and the thickness of 0.01, the lowest natural frequency is found in the second circumferential

Fig. 8 The variation of natural frequencies of the first ten wave numbers of hybrid porous nanocomposite joined shell under different boundary conditions, (**a**) C–C, (**b**) C–F, (**c**) F–C, (**d**) F–F, (**e**) F–S, (**f**) S–F

Table 7 The first mode of the first wave number of pattern-I hybrid porous nanocomposite joined hemispherical–cylindrical–conical versus the different meridional angles of hemispherical under various boundary conditions

| ϑ	Boundary conditions							
	C–C	C-F	C-S	S–S	S-C	S-F	F-S	F–C
0	115.3722	1.2927	111.6348	111.6339	115.3720	0.8931	3.3966	29.5720
10	148.9506	3.8452	148.6443	142.1999	142.3325	1.5254	4.1589	29.7928
20	153.8924	11.4187	153.3314	149.4188	149.6865	3.5393	4.2331	30.2166
30	157.8239	22.2440	157.0744	155.2812	155.7216	5.6344	4.3083	30.9221
40	162.2994	35.4506	161.4616	161.0268	161.6465	7.3426	4.4826	31.9321
50	167.9736	50.2531	167.1518	167.1204	167.9222	8.2504	4.6742	33.2544
60	174.9892	66.4398	174.2658	173.7948	174.7863	8.0444	4.9094	34.9011
70	183.2798	84.5734	182.7122	181.2005	182.3949	6.5704	5.2102	36.8957
80	192.7422	102.1517	192.3212	189.4869	190.8935	3.8269	5.5649	39.2411
90	202.5815	110.8990	202.1488	198.2221	200.3811	1.1084	4.3587	15.4640

wave while this parameter is obtained in the first circumferential wave for other values of shell thickness.

7.6 The effect of semi-vertex angle of the conical part

This example examines the effect of variation of the semi-vertex angle of the conical part on the natural frequency of the hybrid porous nanocomposite joined hemispherical–cylindrical–conical shells. Note that the porosity coefficient of the material is assumed to be 0.1, and the first pattern of porosity distribution is considered. The geometric characteristics of the structure are also taken to be: $R=1$, $L_{cy}=2.5$, $L_{co}=1$.

The results of this study are divided into two steps. At the first step, the effect of the semi-vertex angle of conical on the natural frequency is investigated for two cases. The first case is related to the C–C boundary condition with the shell thickness of 0.01, 0.05, and 0.1. In the second case, the boundary conditions of C–F and F–C are also employed
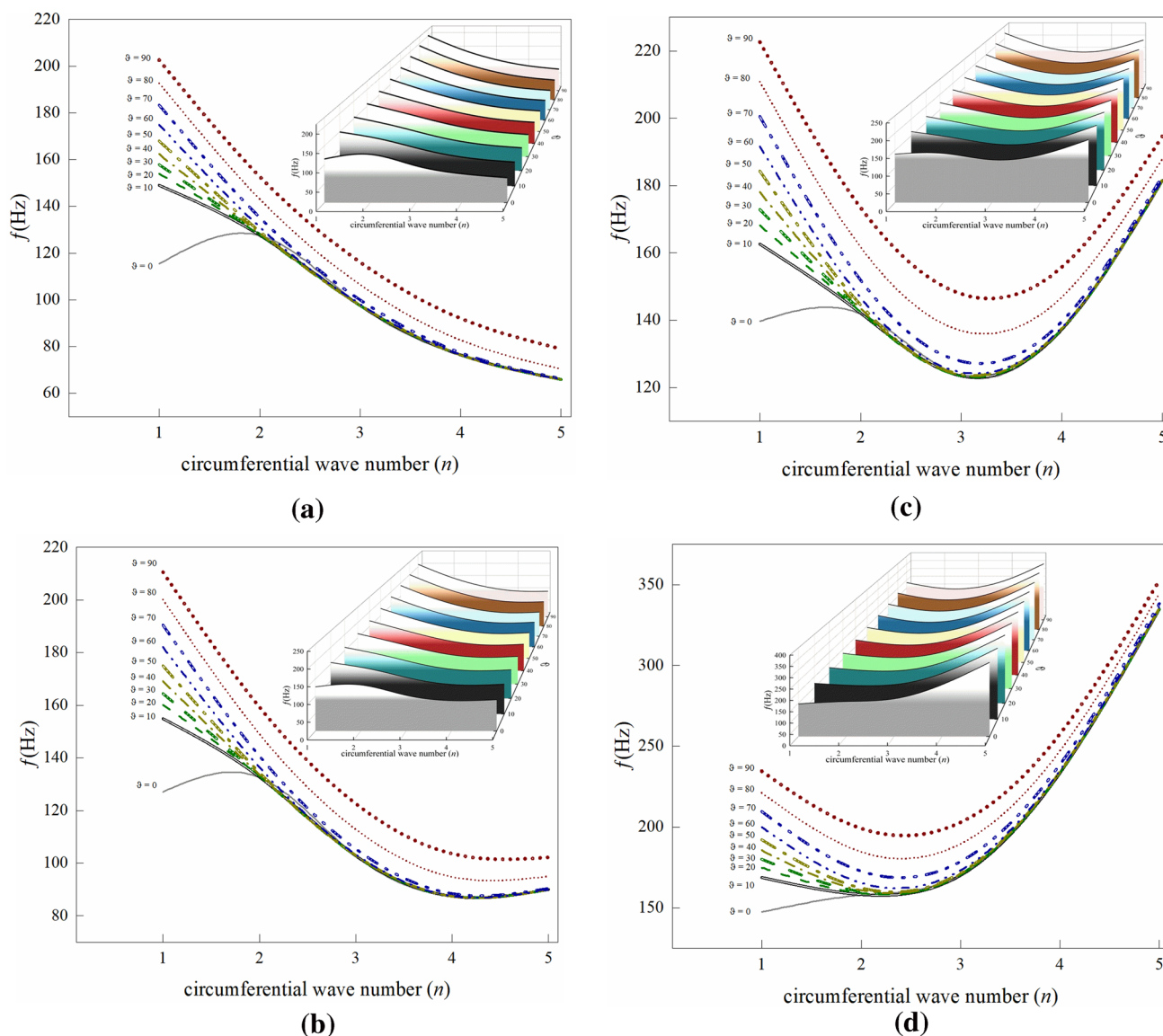
Fig. 9 The variation of natural frequencies of the first five wave numbers versus hemispherical meridional angle with different shell thicknesses, (**a**) thickness = 0.01, (**b**) thickness = 0.02, (**c**) thickness = 0.05, (**d**) thickness = 0.1

Table 8 The first mode of the first wave number of pattern-I hybrid porous nanocomposite joined hemispherical–cylindrical–conical versus different shell thicknesses under various boundary conditions

h	Boundary conditions							
	C–C	C–F	C–S	S–S	S–C	S–F	F–S	F–C
0.01	157.8239	22.2440	157.0744	155.2812	155.7216	5.6344	4.3093	30.9216
0.02	164.3776	24.0483	162.0517	159.6518	161.1285	6.9373	5.1623	31.7953
0.03	168.1191	25.5242	164.5078	161.7624	164.0976	7.8828	5.7657	32.3501
0.04	170.7820	26.8357	166.1339	163.1397	166.1518	8.6610	6.1928	32.8206
0.05	172.8655	28.0334	167.3788	164.1842	167.7254	9.3402	6.6084	33.2898
0.06	174.6010	29.1356	168.4161	165.0492	169.0187	9.9415	6.9568	33.7619
0.07	176.1211	30.1605	169.3312	165.8080	170.1431	10.4990	7.2585	34.2438
0.08	177.5064	31.1148	170.1723	166.5007	171.1638	11.0159	7.5580	34.7333
0.09	178.8072	32.0042	170.1723	167.1500	172.1196	11.4931	7.8471	35.2242
0.1	180.0549	32.8394	171.7382	167.7696	173.0338	11.9491	8.1175	35.7145
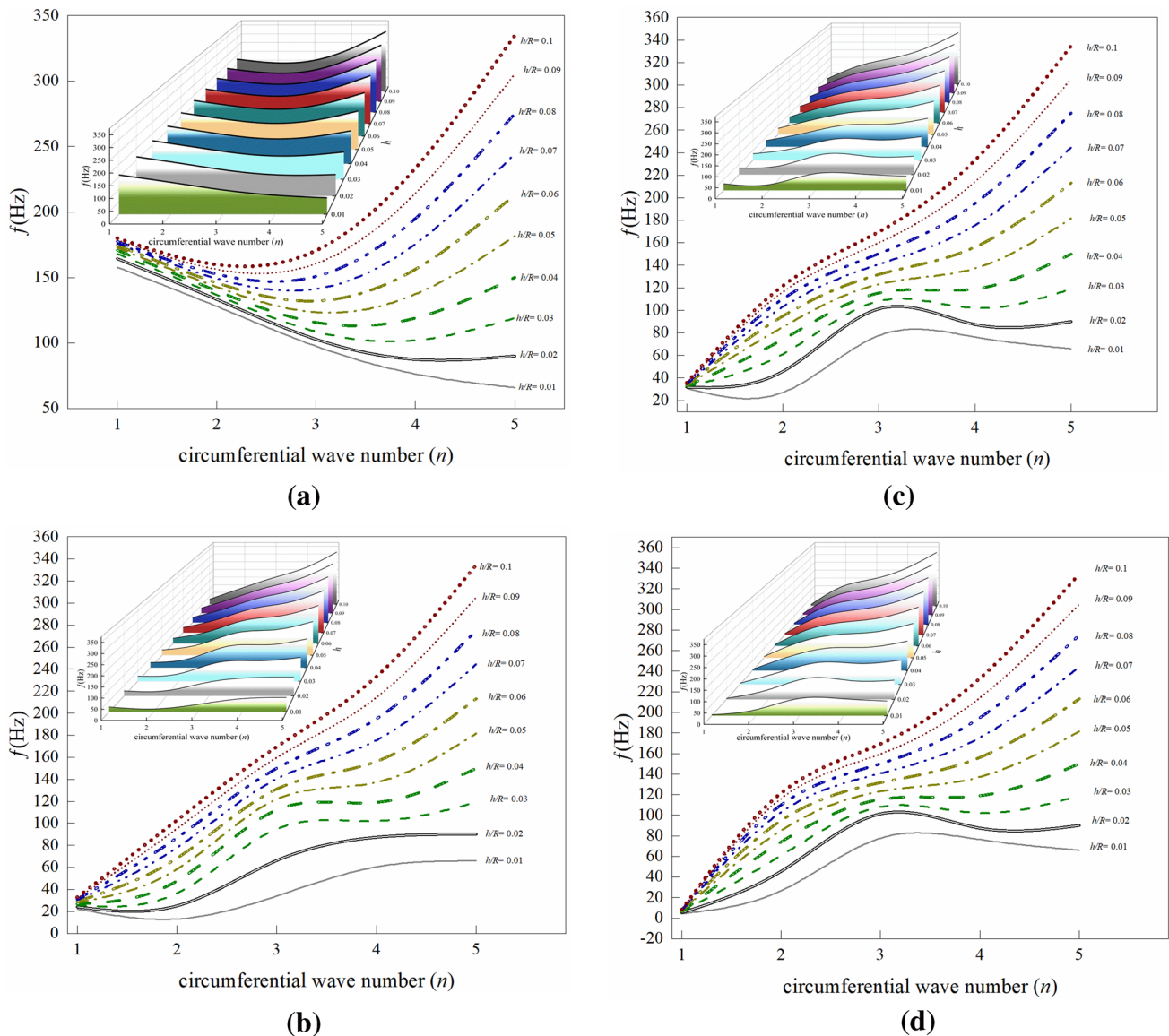
Fig. 10 The variation of the first mode of the first five wave numbers versus various shell thicknesses under different boundary conditions, (**a**) C–C, (**b**) C–F, (**c**) F–C, (**d**) F-S

with the shell thickness of 0.01. The meridional angle of the hemispherical part is taken to be 30°. Figure 11 illustrates the natural frequencies of the structure associated with the first five circumferential waves of the first mode.

It is seen that the highest values of the natural frequency of the shell are found for the case of C–C boundary condition and with the shell thickness of 0.01 in the first, second, third, fourth, and fifth circumferential waves when the semi-vertex angle of the conical part is equal to 50°, 60°, 30°, 20°, and 10°, respectively. On the other hand, the structure with the boundary condition of C–C and shell thickness of 0.05 and 0.1 has the lowest natural frequency in the second, third, fourth, and fifth circumferential waves when the semi-vertex angle of conical is equal to 0°. Furthermore,

the lowest values of the natural frequency of the shell are obtained under the boundary condition of C–F with the shell thickness of 0.01, and the semi-vertex angle of 0° can be obtained at the second, third, fourth, and fifth circumferential waves. In the case of F–C boundary condition and with the shell thickness of 0.01, the highest natural frequency of the structure is found in the first and second circumferential waves when the semi-vertex angle of the conical part is equal to 0°, in the third and fifth circumferential waves when the semi-vertex angle of conical is equal to 10° and in the fourth circumferential wave when the semi-vertex angle of conical is equal to 20°.

At the second step, the natural frequency related to the first circumferential wave of the first mode of the shell under

the boundary conditions of C–C and F–C, with the shell thickness of 0.1 and meridional angle of the hemispherical part of 0°, 30°, 45°, and 60°. The results are presented in Fig. 12.

It is seen that in the cases of C–C and F–C boundary conditions, increasing the meridional angle of the hemispherical part increases the natural frequency of the joined shell. In addition, the highest values of the natural frequency of the joined shell are found in the semi-vertex angle of 20°. In the case of the C–C boundary condition, it is seen that the lowest and highest values of the natural frequency of the joined shell are obtained for the semi-vertex angle of $-90°$ and $+90°$, respectively.

8 Conclusions

This paper was dedicated to studying the free vibration behavior of the hybrid porous nanocomposite joined hemispherical–cylindrical–conical shells composed of three-phase material including a matrix of epoxy, macroscale carbon fiber, and nanoscale 3GFs. The effect of shear deformation was considered using FSDT. The rule of the mixture and Halpin–Tsai homogenization multiscale approaches were employed to, respectively, obtain the equivalent mechanical properties of HM and equivalent material properties of HM reinforced with macroscale carbon fibers. Based on Donnell's shell theory and applying Hamilton's principles, the governing equations of motion related to the joined shells were established. Then, the well-known semi-analytical solution method of GDQM was used to solve the governing differential equations of motion. The procedure of this method was completely presented, and a computer program was developed according to the boundary and coupling conditions. To confirm the proposed formulation, some benchmark problems were solved, and the obtained results were compared with the results of open literature. Furthermore, several new and applicable joined shells were analyzed to investigate the effect of different parameters including material and geometrical properties and boundary conditions on the natural frequencies of hybrid porous nanocomposite joined shells.

Briefly, the following outcomes can be given:

- The natural frequencies of the joined shell decrease with the increasing porosity factor in all patterns.
- Increment of the values of meridional angle of the hemispherical part increases the natural frequency of the joined structure for all values of the shell thickness.
- Increment of the thickness of the structure increases the natural frequency of the shell in all cases.

- Increment of the meridional angle of the hemispherical part increases the natural frequency of the joined shell in the cases of C–C and F–C boundary conditions.

Appendix I

The governing differential equations of joined hemispherical–cylindrical–conical shells in terms of displacement functions are given by
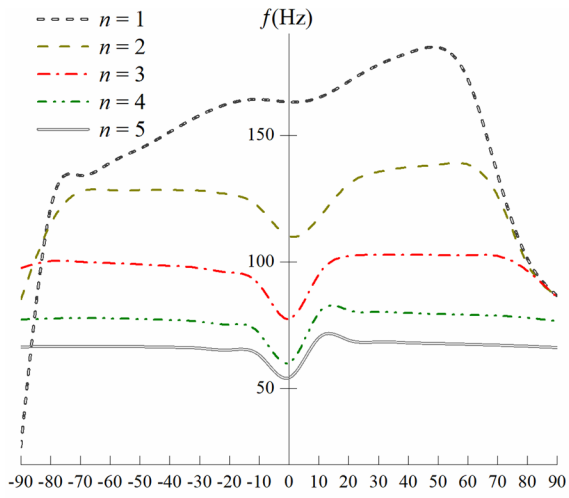
$$\left(\frac{1}{R^2}\right)\{A_{11}\bar{U}^{cy}_{1,\zeta_{cy}\zeta_{cy}}R^2 + \bar{A}_{11}\bar{\Psi}^{cy}_{\zeta,\zeta_{cy}\zeta_{cy}}R^2$$
$$-nR(\bar{A}_{12} + \bar{A}_{66})\bar{\Psi}^{cy}_{\theta,\zeta_{cy}} - nR(A_{12} + A_{66})\bar{U}^{cy}_{2,\zeta_{cy}}$$
$$+RA_{12}\bar{U}^{cy}_{3,\zeta_{cy}} + (\bar{U}^{cy}_1 A_{22} + \bar{\Psi}^{cy}_\zeta \bar{A}_{22})$$
$$-n^2 A_{66}\bar{U}^{cy}_1 - \bar{\Psi}^{cy}_\zeta n^2 \bar{A}_{66}\} = I_1 \omega_n^2 \bar{U}^{cy}_1 + I_2 \omega_n^2 \bar{\Psi}^{cy}_\zeta \tag{71}$$

$$\left(\frac{1}{R^2}\right)\{\bar{A}_{66}\bar{\Psi}^{cy}_{\theta,\zeta_{cy}\zeta_{cy}}R^2 + A_{66}\bar{U}^{cy}_{2,\zeta_{cy}\zeta_{cy}}R^2$$
$$+nR(A_{12} + A_{66})\bar{U}^{cy}_{1,\zeta_{cy}} + nR(\bar{A}_{12} + \bar{A}_{66})\bar{\Psi}^{cy}_{\zeta,\zeta_{cy}}$$
$$-n\bar{U}^{cy}_2(\kappa A_{44} + A_{22}) + n\bar{U}^{cy}_3(\kappa A_{44} + A_{22})\}$$
$$+(-n^2\bar{A}_{22} + R\kappa A_{44})\bar{\Psi}^{cy}_\theta$$
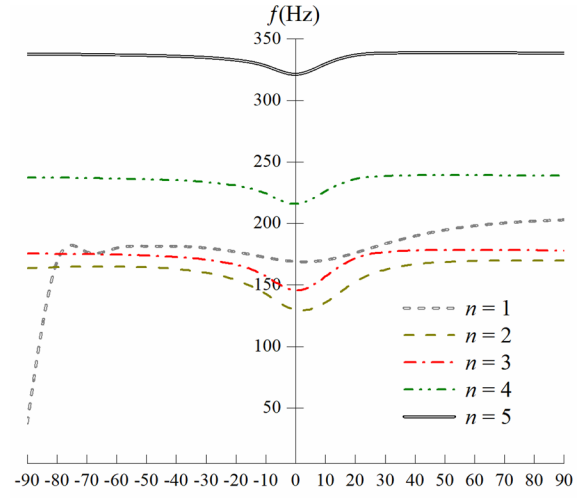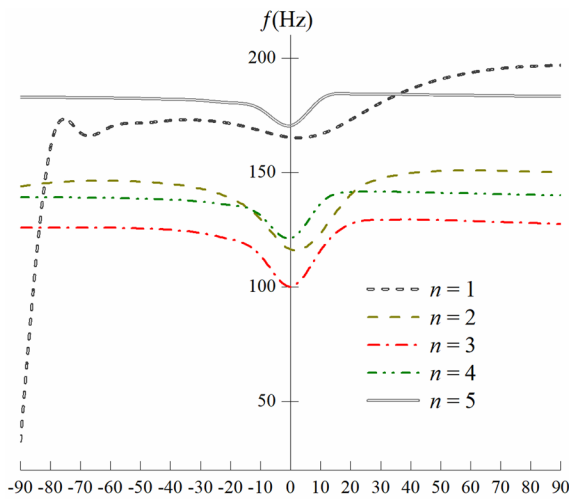$$= I_1 \omega_n^2 \bar{U}^{cy}_2 + I_2 \omega_n^2 \bar{\Psi}^{cy}_\theta \tag{72}$$

$$\left(\frac{1}{R^2}\right)\{\kappa A_{55}R^2\bar{U}^{cy}_{3,\zeta_{cy}\zeta_{cy}} + (R[R\kappa A_{55} - \bar{A}_{12}]\bar{\Psi}^{cy}_{\zeta,\zeta_{cy}}$$
$$-RA_{12}\bar{U}^{cy}_{1,\zeta_{co}} - \bar{U}^{cy}_3 A_{22} - \bar{A}_{22}n\bar{\Psi}^{cy}_\theta$$
$$+\bar{U}^{cy}_2(\kappa A_{44} + A_{22})n$$
$$-((nA_{44}\bar{\Psi}^{cy}_\theta)R + A_{44}n^2\bar{U}^{cy}_3)\kappa\}$$
$$= I_1 \omega_n^2 \bar{U}^{cy}_3 \tag{73}$$

$$\left(\frac{1}{R^2}\right)\{\bar{A}_{11}\bar{U}^{cy}_{1,\zeta_{cy}\zeta_{cy}}R^2 + \bar{\bar{A}}_{11}\bar{\Psi}^{cy}_{\zeta,\zeta_{cy}\zeta_{cy}}R^2$$
$$-nR(\bar{\bar{A}}_{12} + \bar{\bar{A}}_{66})\bar{\Psi}^{cy}_{\theta,\zeta_{cy}} - nR(\bar{A}_{12} + \bar{A}_{66})\bar{U}^{cy}_{2,\zeta_{cy}}$$
$$+(-R^2 A_{55}\kappa + \bar{A}_{12}R)\bar{U}^{cy}_3 - n^2\bar{A}_{66}\bar{U}^{cy}_1$$
$$-R^2 A_{55}\kappa\bar{\Psi}^{cy}_\zeta - \bar{\Psi}^{cy}_\zeta n^2\bar{\bar{A}}_{66}\}$$
$$= I_2 \omega_n^2 \bar{U}^{cy}_1 + I_3 \omega_n^2 \bar{\Psi}^{cy}_\zeta \tag{74}$$

$$\left(\frac{1}{R^2}\right)\{\bar{\bar{A}}_{66}\bar{\Psi}^{cy}_{\theta,\zeta_{cy}\zeta_{cy}}R^2 + \bar{A}_{66}\bar{U}^{cy}_{2,\zeta_{cy}\zeta_{cy}}R^2$$
$$+nR(\bar{A}_{12} + \bar{A}_{66})\bar{U}^{cy}_{1,\zeta_{cy}} + nR(\bar{\bar{A}}_{12} + \bar{\bar{A}}_{66})\bar{\Psi}^{cy}_{\zeta,\zeta_{cy}}$$
$$-R^2\bar{\Psi}^{cy}_\theta \kappa A_{44} - n^2\bar{\bar{A}}_{22}\bar{\Psi}^{cy}_\theta$$
$$-\kappa A_{44}(n\bar{U}^{cy}_3 - \bar{U}^{cy}_2)R - \bar{U}^{cy}_2 n^2\bar{A}_{22}$$
$$+\bar{U}^{cy}_3 n\bar{A}_{22}\} = I_2 \omega_n^2 \bar{U}^{cy}_2 + I_3 \omega_n^2 \bar{\Psi}^{cy}_\theta \tag{75}$$
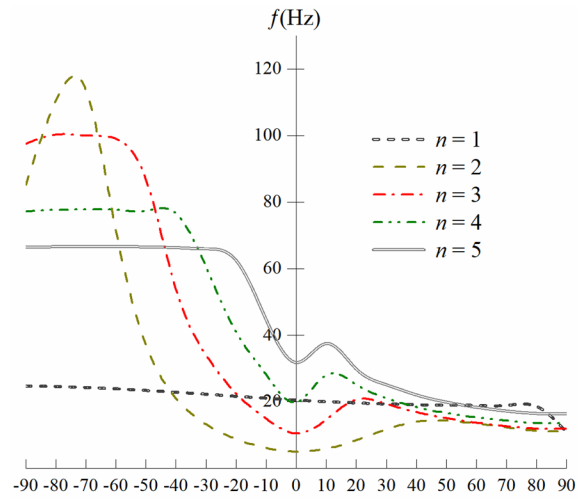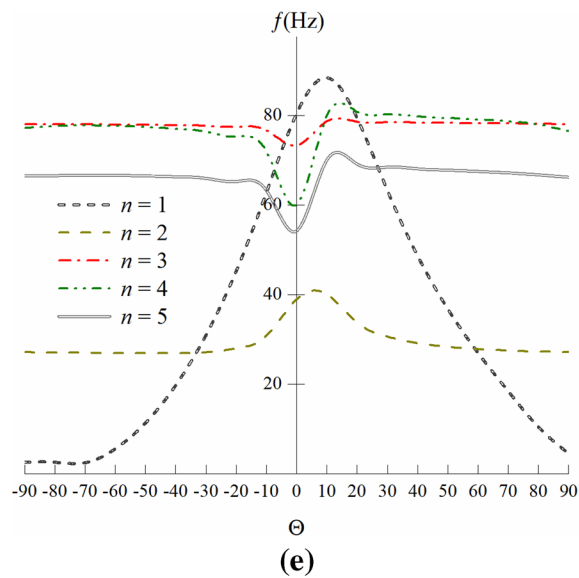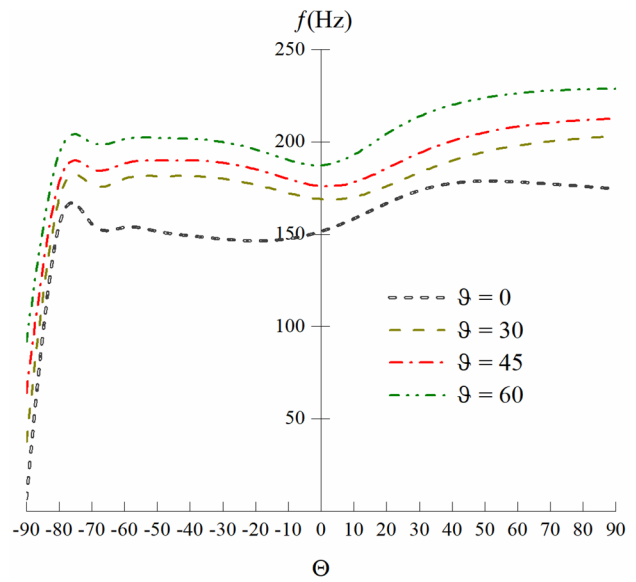
(a)

(b)

(c)

(d)

(e)

◀**Fig. 11** The variation of natural frequencies of the first mode of the first five wave numbers of hybrid porous (pattern-I) nanocomposite joined hemispherical–cylindrical–conical shell in terms of the variation of semi-vertex angle of conical part (**a**) C–C condition and thickness = 0.01, (**b**) C–C condition and thickness = 0.05, (**c**) C–C condition and thickness = 0.1, (**d**) C–F condition and thickness = 0.01, (**e**) F–C condition and thickness = 0.01

$$
\left(\frac{1}{R(\zeta_{co})^2}\right)\{A_{11}\bar{U}^{co}_{1,\zeta_{co}\zeta_{co}}R(\zeta_{co})^2 + \bar{A}_{11}\bar{\Psi}^{co}_{\zeta,\zeta_{co}\zeta_{co}}R(\zeta_{co})^2
$$
$$
-nR(\zeta_{co})(\bar{A}_{12}+\bar{A}_{66})\bar{\Psi}^{co}_{\theta,\zeta_{co}} - nR(\zeta_{co})(A_{12}+A_{66})\bar{U}^{co}_{2,\zeta_{co}}
$$
$$
+\sin(\Theta)R(\zeta_{co})A_{11}\bar{U}^{co}_{1,\zeta_{co}} + \cos(\Theta)R(\zeta_{co})A_{12}\bar{U}^{co}_{3,\zeta_{co}}
$$
$$
+\sin(\Theta)R(\zeta_{co})\bar{A}_{11}\bar{\Psi}^{co}_{\zeta,\zeta_{co}} + (-A_{22}\bar{U}^{co}_{3}\cos(\Theta) + ((\bar{A}_{22}+\bar{A}_{66})\bar{\Psi}^{co}_{\theta}
$$
$$
+\bar{U}^{co}_{2}(A_{22}+A_{66}))n)\sin(\Theta) + (\bar{U}^{co}_{1}A_{22} + \bar{\Psi}^{co}_{\zeta}\bar{A}_{22})\cos(\Theta)^2
$$
$$
+(-n^2A_{66}-A_{22})\bar{U}^{co}_{1} - \bar{\Psi}^{co}_{\zeta}(n^2\bar{A}_{66}+\bar{A}_{22})\} = I_1\omega_n^2\bar{U}^{co}_1 + I_2\omega_n^2\bar{\Psi}^{co}_{\zeta} \tag{76}
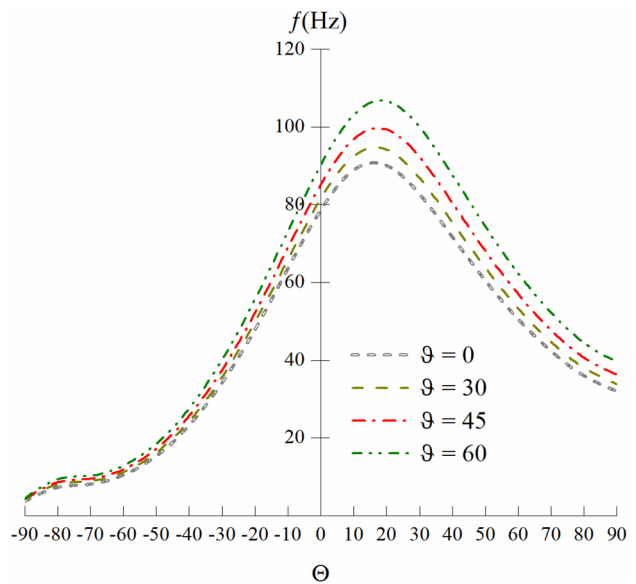$$

$$
\left(\frac{1}{R(\zeta_{co})^2}\right)\{\bar{A}_{66}\bar{\Psi}^{co}_{\theta,\zeta_{co}\zeta_{co}}R(\zeta_{co})^2 + A_{66}\bar{U}^{co}_{2,\zeta_{co}\zeta_{co}}R(\zeta_{co})^2
$$
$$
+nR(\zeta_{co})(A_{12}+A_{66})\bar{U}^{co}_{1,\zeta_{co}} + nR(\zeta_{co})(\bar{A}_{12}+\bar{A}_{66})\bar{\Psi}^{co}_{\zeta,\zeta_{co}}
$$
$$
+\sin(\Theta)R(\zeta_{co})\bar{A}_{66}\bar{\Psi}^{co}_{\theta,\zeta_{co}} + \sin(\Theta)R(\zeta_{co})A_{66}\bar{U}^{co}_{2,\zeta_{co}}
$$
$$
+\cos(\Theta)R(\zeta_{co})\kappa A_{44}\bar{\Psi}^{co}_{\theta} + (\bar{\Psi}^{co}_{\theta}\bar{A}_{66} - \bar{U}^{co}_{2}(\kappa A_{44}-A_{66}))\cos(\Theta)^2
$$
$$
+n\bar{U}^{co}_{2}(\kappa A_{44}+A_{22})\cos(\Theta) + n((A_{22}+A_{66})\bar{U}^{co}_{1}
$$
$$
+\bar{\Psi}^{co}_{\zeta}(\bar{A}_{22}+\bar{A}_{66}))\sin(\Theta) + (-n^2\bar{A}_{22}-\bar{A}_{66})\bar{\Psi}^{co}_{\theta} - \bar{U}^{co}_{2}(n^2A_{22}+A_{66})\}
$$
$$
= I_1\omega_n^2\bar{U}^{co}_2 + I_2\omega_n^2\bar{\Psi}^{co}_{\theta} \tag{77}
$$

$$
\left(\frac{1}{R(\zeta_{co})^2}\right)\{\kappa A_{55}R(\zeta_{co})^2\bar{U}^{co}_{3,\zeta_{co}\zeta_{co}}
$$
$$
+ (R(\zeta_{co})[R(\zeta_{co})\kappa A_{55} - \bar{A}_{12}\cos(\Theta))\bar{\Psi}^{co}_{\zeta,\zeta_{co}}
$$
$$
- R(\zeta_{co})\cos(\Theta)A_{12}\bar{U}^{co}_{1,\zeta_{co}} + \sin(\Theta)R(\zeta_{co})\kappa A_{55}\bar{U}^{co}_{3,\zeta_{co}}
$$
$$
- \bar{U}^{co}_{3}\cos(\Theta)^2A_{22} + ((-A_{22}\bar{U}^{co}_{1} - \bar{A}_{22}\bar{\Psi}^{co}_{\zeta})\sin(\Theta)
$$
$$
+ (\bar{A}_{22}\bar{\Psi}^{co}_{\theta} + \bar{U}^{co}_{2}(\kappa A_{44}+A_{22}))n)\cos(\Theta)
$$
$$
- ((nA_{44}\bar{\Psi}^{co}_{\theta} - A_{44}\bar{\Psi}^{co}_{\zeta}\sin(\Theta))R(\zeta_{co}) + n^2\bar{U}^{co}_{3})\kappa\}
$$
$$
= I_1\omega_n^2\bar{U}^{co}_3 \tag{78}
$$

$$
\left(\frac{1}{R(\zeta_{co})^2}\right)\{\bar{A}_{11}\bar{U}^{co}_{1,\zeta_{co}\zeta_{co}}R(\zeta_{co})^2 + \bar{\bar{A}}_{11}\bar{\Psi}^{co}_{\zeta,\zeta_{co}\zeta_{co}}R(\zeta_{co})^2
$$
$$
- nR(\zeta_{co})(\bar{\bar{A}}_{12}+\bar{\bar{A}}_{66})\bar{\Psi}^{co}_{\theta,\zeta_{co}} - nR(\zeta_{co})(\bar{A}_{12}+\bar{A}_{66})\bar{U}^{co}_{2,\zeta_{co}}
$$
$$
+ (-R(\zeta_{co})^2A_{55}\kappa + \bar{A}_{12}\cos(\Theta)R(\zeta_{co}))\bar{U}^{co}_{3}
$$
$$
+ \sin(\Theta)R(\zeta_{co})\bar{A}_{11}\bar{U}^{co}_{1,\zeta_{co}} + \sin(\Theta)R(\zeta_{co})\bar{\bar{A}}_{11}\bar{\Psi}^{co}_{\zeta,\zeta_{co}} \tag{79}
$$
$$
- R(\zeta_{co})^2A_{55}\kappa\bar{\Psi}^{co}_{\zeta} + (-\bar{A}_{22}\bar{U}^{co}_{3}\cos(\Theta)
$$
$$
+ ((\bar{\bar{A}}_{22}+\bar{\bar{A}}_{66})\bar{\Psi}^{co}_{\theta} + \bar{U}^{co}_{2}(\bar{A}_{22}+\bar{A}_{66}))n)\sin(\Theta)
$$
$$
+ (\bar{U}^{co}_{1}\bar{A}_{22} + \bar{\Psi}^{co}_{\zeta}\bar{\bar{A}}_{22})\cos(\Theta)^2
$$
$$
- (n^2A_{66}+A_{22})\bar{U}^{co}_{1} + \bar{\Psi}^{co}_{\zeta}(-n^2\bar{\bar{A}}_{66}-\bar{\bar{A}}_{22})\}
$$
$$
= I_2\omega_n^2\bar{U}^{co}_1 + I_3\omega_n^2\bar{\Psi}^{co}_{\zeta}
$$

f(Hz)

(**a**)

f(Hz)

(**b**)

Fig. 12 The variation of the first mode of the first wave numbers of hybrid porous (pattern-I) nanocomposite joined shell in terms of variation of semi-vertex angle of conical versus different hemispherical meridional angle with shell thickness equal to 0.1, (**a**) C–C, (**b**) F–C

$$\left(\frac{1}{R(\zeta_{co})^2}\right)\{\bar{\bar{A}}_{66}\bar{\Psi}^{co}_{\theta,\zeta_{co}\zeta_{co}}R(\zeta_{co})^2 + \bar{A}_{66}\bar{U}^{co}_{2,\zeta_{co}\zeta_{co}}R(\zeta_{co})^2$$

$$+nR(\zeta_{co})(\bar{A}_{12}+\bar{A}_{66})\bar{U}^{co}_{1,\zeta_{co}} + nR(\zeta_{co})(\bar{\bar{A}}_{12}+\bar{\bar{A}}_{66})\bar{\Psi}^{co}_{\zeta,\zeta_{co}}$$

$$+\sin(\Theta)R(\zeta_{co})\bar{\bar{A}}_{66}\bar{\Psi}^{co}_{\theta,\zeta_{co}} + \sin(\Theta)R(\zeta_{co})\bar{A}_{66}\bar{U}^{co}_{2,\zeta_{co}}$$

$$-R(\zeta_{co})^2\bar{\Psi}^{co}_{\theta}\kappa A_{44} - \kappa A_{44}(n\bar{U}^{co}_3 - \cos(\Theta)\bar{U}^{co}_2)R(\zeta_{co})$$

$$+n((\bar{A}_{22}+\bar{A}_{66})\bar{U}^{co}_1 + \bar{\Psi}^{co}_{\zeta}(\bar{\bar{A}}_{22}+\bar{\bar{A}}_{66})\sin(\Theta)$$

$$+(\bar{\Psi}^{co}_{\theta}\bar{\bar{A}}_{66} + \bar{U}^{co}_2(\bar{A}_{66})\cos(\Theta)^2 + \cos(\Theta)\bar{U}^{co}_3 n\bar{A}_{22}$$

$$+(-n^2\bar{\bar{A}}_{22} - \bar{\bar{A}}_{66})\bar{\Psi}^{co}_{\theta} - \bar{U}^{co}_2(n^2\bar{A}_{22}+\bar{A}_{66})\}$$

$$= I_2\omega_n^2\bar{U}^{co}_2 + I_3\omega_n^2\bar{\Psi}^{co}_{\theta}$$

$$(80)$$

$$\left(\frac{1}{R^2\sin(\zeta_{hs})^2}\right)\{(-\cos(\zeta_{hs})^2 A_{11}+A_{11})\bar{U}^{hs}_{1,\zeta_{hs}\zeta_{hs}} + (-\cos(\zeta_{hs})^2\bar{A}_{11}+\bar{A}_{11})\bar{\Psi}^{hs}_{\zeta,\zeta_{hs}\zeta_{hs}}$$

$$-(\cos(\zeta_{hs})^2-1)(\kappa A_{55}+A_{11}+A_{12})\bar{U}^{hs}_{3,\zeta_{hs}} - n\sin(\zeta_{hs})(\bar{A}_{12}+\bar{A}_{66})\bar{\Psi}^{hs}_{\theta,\zeta_{hs}}$$

$$-n\sin(\zeta_{hs})(\bar{A}_{12}+\bar{A}_{66})\bar{U}^{hs}_{2,\zeta_{hs}} + \sin(\zeta_{hs})\cos(\zeta_{hs})A_{11}\bar{U}^{hs}_{1,\zeta_{hs}}$$

$$+\sin(\zeta_{hs})\cos(\zeta_{hs})\bar{A}_{11}\bar{\Psi}^{hs}_{\zeta,\zeta_{hs}} + ((\kappa A_{55}+A_{12}-A_{22})\bar{U}^{hs}_1$$

$$+\bar{\Psi}^{hs}_{\zeta}(-\kappa A_{55}R+\bar{A}_{12}-\bar{A}_{22}))\cos(\zeta_{hs})^2 + (\bar{U}^{hs}_3(A_{11}+A_{22})\sin(\zeta_{hs})$$

$$+((\bar{A}_{22}+\bar{A}_{66})\bar{\Psi}^{hs}_{\theta} + \bar{U}^{hs}_2(A_{22}+A_{66})n)\cos(\zeta_{hs})+$$

$$(-n^2 A_{66}-\kappa A_{55}-A_{12})\bar{U}^{hs}_1 - \bar{\Psi}^{hs}_{\zeta}(-\kappa A_{55}R+n^2\bar{A}_{66}+\bar{A}_{12})\}$$

$$= I_1\omega_n^2\bar{U}^{hs}_1 + I_2\omega_n^2\bar{\Psi}^{hs}_{\zeta}$$

$$(81)$$

$$\left(\frac{1}{R^2\sin(\zeta_{hs})^2}\right)\{(-\cos(\zeta_{hs})^2\bar{A}_{66}+\bar{A}_{66})\bar{\Psi}^{hs}_{\theta,\zeta_{hs}\zeta_{hs}} + (-\cos(\zeta_{hs})^2 A_{66}+A_{66})\bar{U}^{hs}_{2,\zeta_{hs}\zeta_{hs}}$$

$$+n\sin(\zeta_{hs})(A_{12}+A_{66})\bar{U}^{hs}_{1,\zeta_{hs}} + n\sin(\zeta_{hs})(\bar{A}_{12}+\bar{A}_{66})\bar{\Psi}^{hs}_{\zeta,\zeta_{hs}}$$

$$+\sin(\zeta_{hs})\cos(\zeta_{hs})\bar{A}_{66}\bar{\Psi}^{hs}_{\theta,\zeta_{hs}} + \sin(\zeta_{hs})\cos(\zeta_{hs})A_{66}\bar{U}^{hs}_{2,\zeta_{hs}}$$

$$+((-\kappa A_{44}R - 2\bar{A}_{66})\bar{\Psi}^{hs}_{\theta} + \bar{U}^{hs}_2(\kappa A_{44}-2A_{66}))\cos(\zeta_{hs})^2$$

$$+((A_{22}+A_{66})\bar{U}^{hs}_1 + \bar{\Psi}^{hs}_{\zeta}(\bar{A}_{22}+\bar{A}_{66}))n\cos(\zeta_{hs})+$$

$$n\bar{U}^{hs}_3(\kappa A_{44}+A_{12}+A_{22})\sin(\zeta_{hs}) + (\kappa A_{44}R - n^2\bar{A}_{22}+\bar{A}_{66})\bar{\Psi}^{hs}_{\theta}$$

$$-\bar{U}^{hs}_2(n^2 A_{22}+\kappa A_{44}-A_{66})\} = I_1\omega_n^2\bar{U}^{hs}_2 + I_2\omega_n^2\bar{\Psi}^{hs}_{\theta}$$

$$(82)$$

$$\left(\frac{1}{R^2\sin(\zeta_{hs})^2}\right)\{(-\cos(\zeta_{hs})^2\kappa A_{55}+\kappa A_{55})\bar{U}^{hs}_{3,\zeta_{hs}\zeta_{hs}}$$

$$+(\cos(\zeta_{hs})^2-1)(\kappa A_{55}+A_{11}+A_{12})\bar{U}^{hs}_{1,\zeta_{hs}}$$

$$+(\cos(\zeta_{hs})^2-1)(-\kappa A_{55}R+\bar{A}_{11}+\bar{A}_{12})\bar{\Psi}^{hs}_{\zeta,\zeta_{hs}}$$

$$+\sin(\zeta_{hs})\cos(\zeta_{hs})\kappa A_{55}\bar{U}^{hs}_{3,\zeta_{hs}} + \bar{U}^{hs}_3(A_{11}+2A_{12}+A_{22})\cos(\zeta_{hs})^2$$

$$-((\kappa A_{55}+A_{22}+A_{12})\bar{U}^{hs}_1 + \bar{\Psi}^{hs}_{\zeta}(-\kappa A_{55}R+\bar{A}_{22}+\bar{A}_{12}))\sin(\zeta_{hs})\cos(\zeta_{hs})$$

$$+n((-\kappa A_{44}R+\bar{A}_{22}+\bar{A}_{12})\bar{\Psi}^{hs}_{\theta} + \bar{U}^{hs}_2(\kappa A_{44}+A_{12}+A_{22}))\sin(\zeta_{hs})$$

$$-\bar{U}^{hs}_3(\kappa n^2 A_{44}+A_{11}+2A_{12}+A_{22})\} = I_1\omega_n^2\bar{U}^{hs}_3$$

$$(83)$$

$$\left(\frac{1}{R^2 \sin(\zeta_{hs})^2}\right)\{(-\cos(\zeta_{hs})^2 \bar{A}_{11} + \bar{A}_{11})\bar{U}_{1,\zeta_{hs}\zeta_{hs}}^{hs} + (-\cos(\zeta_{hs})^2 \bar{\bar{A}}_{11} + \bar{\bar{A}}_{11})\bar{\Psi}_{\zeta,\zeta_{hs}\zeta_{hs}}^{hs}$$

$$+(\cos(\zeta_{hs})^2 - 1)(\kappa A_{55}R + \bar{A}_{11} + \bar{\bar{A}}_{12})\bar{U}_{3,\zeta_{hs}}^{hs} - n\sin(\zeta_{hs})(\bar{\bar{A}}_{12} + \bar{\bar{A}}_{66})\bar{\Psi}_{\theta,\zeta_{hs}}^{hs}$$

$$-n\sin(\zeta_{hs})(\bar{A}_{12} + \bar{\bar{A}}_{66})\bar{U}_{2,\zeta_{hs}}^{hs} + \sin(\zeta_{hs})\cos(\zeta_{hs})\bar{A}_{11}\bar{U}_{1,\zeta_{hs}}^{hs}$$

$$+\sin(\zeta_{hs})\cos(\zeta_{hs})\bar{\bar{A}}_{11}\bar{\Psi}_{\zeta,\zeta_{hs}}^{hs} + ((\kappa A_{55}R + \bar{A}_{12} - \bar{A}_{22})\bar{U}_1^{hs}$$

$$+\bar{\Psi}_\zeta^{hs}(-\kappa A_{55}R^2 + \bar{\bar{A}}_{12} - \bar{\bar{A}}_{22}))\cos(\zeta_{hs})^2 + (\bar{U}_3^{hs}(\bar{A}_{11} + \bar{A}_{22})\sin(\zeta_{hs})$$

$$+n((\bar{\bar{A}}_{22} + \bar{\bar{A}}_{66})\bar{\Psi}_\theta^{hs} + \bar{U}_2^{hs}(\bar{A}_{22} + \bar{A}_{66})))\cos(\zeta_{hs})+$$

$$(-n^2\bar{A}_{66} - \kappa A_{55}R - \bar{A}_{12})\bar{U}_1^{hs} - \bar{\Psi}_\zeta^{hs}(-\kappa A_{55}R^2 + n^2\bar{\bar{A}}_{66} + \bar{\bar{A}}_{12})\}$$

$$= I_2\omega_n^2\bar{U}_1^{hs} + I_3\omega_n^2\bar{\Psi}_\zeta^{hs} \tag{84}$$

$$\left(\frac{1}{R^2 \sin(\zeta_{hs})^2}\right)\{(-\cos(\zeta_{hs})^2 \bar{\bar{A}}_{66} + \bar{\bar{A}}_{66})\bar{\Psi}_{\theta,\zeta_{hs}\zeta_{hs}}^{hs} + (-\cos(\zeta_{hs})^2 \bar{A}_{66} + A_{66})\bar{U}_{2,\zeta_{hs}\zeta_{hs}}^{hs}$$

$$+n\sin(\zeta_{hs})(\bar{A}_{12} + \bar{A}_{66})\bar{U}_{1,\zeta_{hs}}^{hs} + n\sin(\zeta_{hs})(\bar{\bar{A}}_{12} + \bar{\bar{A}}_{66})\bar{\Psi}_{\zeta,\zeta_{hs}}^{hs}$$

$$+\sin(\zeta_{hs})\cos(\vartheta)\bar{\bar{A}}_{66}\bar{\Psi}_{\theta,\zeta_{hs}}^{hs} + \sin(\zeta_{hs})\cos(\vartheta\zeta_{hs})\bar{A}_{66}\bar{U}_{2,\zeta_{hs}}^{hs}$$

$$+((-\kappa A_{44}R^2 - 2\bar{\bar{A}}_{66})\bar{\Psi}_\theta^{hs} - \bar{U}_2^{hs}(\kappa A_{44}R + 2A_{66}))\cos(\zeta_{hs})^2$$

$$+((\bar{A}_{22} + \bar{A}_{66})\bar{U}_1^{hs} + \bar{\Psi}_\zeta^{hs}(\bar{\bar{A}}_{22} + \bar{\bar{A}}_{66}))n\cos(\zeta_{hs})-$$

$$n\bar{U}_3^{hs}(\kappa A_{44}R - \bar{A}_{12} - \bar{A}_{22})\sin(\zeta_{hs}) + (-\kappa A_{44}R^2 - n^2\bar{\bar{A}}_{22} + \bar{\bar{A}}_{66})\bar{\Psi}_\theta^{hs}$$

$$-\bar{U}_2^{hs}(n^2 A_{22} - \kappa A_{44}R - A_{66})\} = I_2\omega_n^2\bar{U}_2^{hs} + I_3\omega_n^2\bar{\Psi}_\theta^{hs} \tag{85}$$

Declarations

References

1. Mashat DS, Carrera E, Zenkour AM, Al Khateeb SA (2014) Use of axiomatic/asymptotic approach to evaluate various refined theories for sandwich shells. Compos Struct 109:139–149. https://doi.org/10.1016/j.compstruct.2013.10.046

2. Kamarian S, Salim M, Dimitri R, Tornabene F (2016) Free vibration analysis of conical shells reinforced with agglomerated Carbon Nanotubes. Int J Mech Sci 108–109:157–165. https://doi.org/10.1016/j.ijmecsci.2016.02.006

3. Heydarpour Y, Malekzadeh P, Dimitri R, Tornabene F (2020) Thermoelastic analysis of rotating multilayer FG-GPLRC truncated conical shells based on a coupled TDQM-NURBS scheme. Compos Struct 235:111707. https://doi.org/10.1016/j.compstruct.2019.111707

4. Dewangan HC, Panda SK (2020) Numerical thermoelastic eigenfrequency prediction of damaged layered shell panel with concentric/eccentric cutout and corrugated (TD/TID) properties. Eng Comput 1:3. https://doi.org/10.1007/s00366-020-01199-1

5. Khadimallah MA, Hussain M, Khedher KM, et al (2020) Backward and forward rotating of FG ring support cylindrical shells. Steel Compos Struct 37:137–150. https://doi.org/10.12989/scs.2020.37.2.137

6. Rostami R, Mohammadimehr M (2020) Vibration control of rotating sandwich cylindrical shell-reinforced nanocomposite face sheet and porous core integrated with functionally graded magneto-electro-elastic layers. Eng Comput 1:3. https://doi.org/10.1007/s00366-020-01052-5

7. Sangtarash H, Arab HG, Sohrabi MR, Ghasemi MR (2020) Formulation and evaluation of a new four-node quadrilateral element for analysis of the shell structures. Eng Comput 36:1289–1303. https://doi.org/10.1007/s00366-019-00763-8

8. Shamloofard M, Hosseinzadeh A, Movahhedy MR (2020) Development of a shell superelement for large deformation and free vibration analysis of composite spherical shells. Eng Comput 1–17. https://doi.org/10.1007/s00366-020-01015-w

9. Shen HS, Li C, Reddy JN (2020) Large amplitude vibration of FG-CNTRC laminated cylindrical shells with negative Poisson's ratio. Comput Methods Appl Mech Eng 360:112727. https://doi.org/10.1016/j.cma.2019.112727

10. Hirwani CK, Mishra PK, Panda SK (2021) Nonlinear steadystate responses of weakly bonded composite shell structure under hygro-thermo-mechanical loading. Compos Struct 265:113768. https://doi.org/10.1016/j.compstruct.2021.113768

11. Mehar K, Mishra PK, Panda SK (2021) Thermal buckling strength of smart nanotube-reinforced doubly curved hybrid composite panels. Comput Math with Appl 90:13–24. https://doi.org/10.1016/j.camwa.2021.03.010

12. Mehar K, Mishra PK, Panda SK (2021) Thermal post-buckling strength prediction and improvement of shape memory alloy bonded carbon nanotube-reinforced shallow shell panel: a nonlinear finite element micromechanical approach. J Press Vessel Technol 143:. https://doi.org/10.1115/1.4050934

13. Hirwani CK, Panda SK, Mahapatra TR, Mahapatra SS (2017) Numerical study and experimental validation of dynamic characteristics of delaminated composite flat and curved shallow shell structure. J Aerosp Eng 30:04017045. https://doi.org/10.1061/(asce)as.1943-5525.0000756

14. Patnaik SS, Roy T (2021) Vibration and damping characteristics of CNTR viscoelastic skewed shell structures under the influence of hygrothermal conditions. Eng Comput 1:3. https://doi.org/10.1007/s00366-021-01411-w

15. Tornabene F, Viscoti M, Dimitri R, Reddy JN (2021) Higher order theories for the vibration study of doubly-curved anisotropic shells with a variable thickness and isogeometric mapped geometry. Compos Struct 267:113829. https://doi.org/10.1016/j.compstruct.2021.113829

16. Zine A, Tounsi A, Draiche K, et al (2018) A novel higher-order shear deformation theory for bending and free vibration analysis of isotropic and multilayered plates and shells. Steel Compos Struct 26:125–137. https://doi.org/10.12989/scs.2018.26.2.125

17. Barati MR, Zenkour AM (2019) Vibration analysis of functionally graded graphene platelet reinforced cylindrical shells with different porosity distributions. Mech Adv Mater Struct 26:1580–1588. https://doi.org/10.1080/15376494.2018.1444235

18. Ebrahimi F, Habibi M, Safarpour H (2019) On modeling of wave propagation in a thermally affected GNP-reinforced imperfect nanocomposite shell. Eng Comput 35:1375–1389. https://doi.org/10.1007/s00366-018-0669-4

19. Bisheh H, Wu N, Rabczuk T (2019) Free vibration analysis of smart laminated carbon nanotube-reinforced composite cylindrical shells with various boundary conditions in hygrothermal environments. Thin-Walled Struct 149:106500. https://doi.org/10.1016/j.tws.2019.106500

20. Katariya PV, Panda SK (2019) Numerical evaluation of transient deflection and frequency responses of sandwich shell structure using higher order theory and different mechanical loadings. Eng Comput 35:1009–1026. https://doi.org/10.1007/s00366-018-0646-y

21. Amabili M, Reddy JN (2020) The nonlinear, third-order thickness and shear deformation theory for statics and dynamics of laminated composite shells. Compos Struct 244:112265. https://doi.org/10.1016/j.compstruct.2020.112265

22. Bisheh H, Rabczuk T, Wu N (2020) Effects of nanotube agglomeration on wave dynamics of carbon nanotube-reinforced piezo-composite cylindrical shells. Compos Part B Eng 187:107739. https://doi.org/10.1016/j.compositesb.2019.107739

23. Rezaiee-Pajand M, Masoodi AR, Arabi E (2018) On the shell thickness-stretching effects using seven-parameter triangular element. Eur J Comput Mech 27:163–185. https://doi.org/10.1080/17797179.2018.1484208

24. Rezaiee-Pajand M, Arabi E, Masoodi AR (2018) A triangular shell element for geometrically nonlinear analysis. Acta Mech 229:323–342. https://doi.org/10.1007/s00707-017-1971-8

25. Masoodi AR, Arabi E (2018) Geometrically nonlinear thermomechanical analysis of shell-like structures. J Therm Stress 41:37–53. https://doi.org/10.1080/01495739.2017.1360166

26. Żur KK (2018) Quasi-Green's function approach to free vibration analysis of elastically supported functionally graded circular plates. Compos Struct 183:600–610. https://doi.org/10.1016/j.compstruct.2017.07.012

27. Żur KK (2019) Free-vibration analysis of discrete-continuous functionally graded circular plate via the Neumann series method. Appl Math Model 73:166–189. https://doi.org/10.1016/j.apm.2019.02.047

28. Sharma N, Lalepalli AK, Hirwani CK et al (2021) Optimal deflection and stacking sequence prediction of curved composite structure using hybrid (FEM and soft computing) technique. Eng Comput 37:477–487. https://doi.org/10.1007/s00366-019-00836-8

29. Liew KM, Ng TY, Zhao X (2005) Free vibration analysis of conical shells via the element-free kp-Ritz method. J Sound Vib 281:627–645. https://doi.org/10.1016/j.jsv.2004.01.005

30. Irie T, Yamada G, Kaneko Y (1982) Free vibration of a conical shell with variable thickness. J Sound Vib 82:83–94. https://doi.org/10.1016/0022-460X(82)90544-2

31. Civalek Ö (2006) An efficient method for free vibration analysis of rotating truncated conical shells. Int J Press Vessel Pip 83:1–12. https://doi.org/10.1016/j.ijpvp.2005.10.005

32. Bellman R, Kashef BG, Casti J (1972) Differential quadrature: a technique for the rapid solution of nonlinear partial differential equations. J Comput Phys 10:40–52. https://doi.org/10.1016/0021-9991(72)90089-7

33. Shu C, Richards BE (1992) Application of generalized differential quadrature to solve two-dimensional incompressible Navier–Stokes equations. Int J Numer Methods Fluids 15:791–798. https://doi.org/10.1002/fld.1650150704

34. Al-Furjan MSH, Safarpour H, Habibi M et al (2020) A comprehensive computational approach for nonlinear thermal instability of the electrically FG-GPLRC disk based on GDQ method. Eng Comput 1:3. https://doi.org/10.1007/s00366-020-01088-7

35. Al-Furjan MSH, Habibi M, Rahimi A et al (2020) Chaotic simulation of the multi-phase reinforced thermo-elastic disk using GDQM. Eng Comput 1:3. https://doi.org/10.1007/s00366-020-01144-2

36. Al-Furjan MSH, Habibi M, Ni J et al (2020) Frequency simulation of viscoelastic multi-phase reinforced fully symmetric systems. Eng Comput 1:3. https://doi.org/10.1007/s00366-020-01200-x

37. Al-Furjan MSH, Hatami A, Habibi M et al (2021) On the vibrations of the imperfect sandwich higher-order disk with a lactic core using generalize differential quadrature method. Compos Struct 257:113150. https://doi.org/10.1016/j.compstruct.2020.113150

38. Du H, Lim MK, Lin RM (1994) Application of generalized differential quadrature method to structural problems. Int J Numer Methods Eng 37:1881–1896. https://doi.org/10.1002/nme.1620371107

39. Shu C (1996) An efficient approach for free vibration analysis of conical shells. Int J Mech Sci 38:935–949. https://doi.org/10.1016/0020-7403(95)00096-8

40. Bagheri H, Kiani Y, Eslami MR (2017) Free vibration of conical shells with intermediate ring support. Aerosp Sci Technol 69:321–332. https://doi.org/10.1016/j.ast.2017.06.037

41. Penzes LE, Kraus H (1972) Free vibration of prestressed cylindrical shells having arbitrary homogeneous boundary conditions. AIAA J 10:1309–1313. https://doi.org/10.2514/3.6605

42. Loy CT, Lam KY (1997) Vibration of cylindrical shells with ring support. Int J Mech Sci 39:455–471. https://doi.org/10.1016/s0020-7403(96)00035-5

43. Xiang Y, Ma YF, Kitipornchai S et al (2002) Exact solutions for vibration of cylindrical shells with intermediate ring supports. Int J Mech Sci 44:1907–1924. https://doi.org/10.1016/S0020-7403(02)00071-1

44. Saunders H, Wisniewski EJ, Paslay PR (1960) Vibrations of Conical Shells. J Acoust Soc Am 32:765–772. https://doi.org/10.1121/1.1908207

45. Weingarten VI (1965) Free vibrations of ring-stiffened conical shells. AIAA J 3:1475–1481. https://doi.org/10.2514/3.3171

46. Srinivasan RS, Krishnan PA (1987) Free vibration of conical shell panels. J Sound Vib 117:153–160. https://doi.org/10.1016/0022-460X(87)90441-X

47. Ross CTF, Sawkins D, Johns T (1999) Inelastic buckling of thick-walled circular conical shells under external hydrostatic pressure. Ocean Eng 26:1297–1310. https://doi.org/10.1016/S0029-8018(98)00066-3

48. Ross CTF, Little APF, Adeniyi KA (2005) Plastic buckling of ring-stiffened conical shells under external hydrostatic pressure. Ocean Eng 32:21–36. https://doi.org/10.1016/j.oceaneng.2004.05.007

49. Chen M, Xie K, Jia W, Xu K (2015) Free and forced vibration of ring-stiffened conical-cylindrical shells with arbitrary boundary conditions. Ocean Eng 108:241–256. https://doi.org/10.1016/j.oceaneng.2015.07.065

50. Xie D, Zhang C (2020) Study on transverse vibration characteristics of the coupled system of shaft and submerged conical-cylindrical shell. Ocean Eng 197:. https://doi.org/10.1016/j.oceaneng.2019.106834

51. Lam KY, Li H, Ng TY, Chua CF (2002) Generalized differential quadrature method for the free vibration of truncated conical panels. J Sound Vib 251:329–348. https://doi.org/10.1006/jsvi.2001.3993

52. Lam KY, Hua L (2000) Influence of initial pressure on frequency characteristics of a rotating truncated circular conical shell. Int J Mech Sci 42:213–236. https://doi.org/10.1016/S0020-7403(98)00125-8

53. Li H, Lam KY (2000) The generalized differential quadrature method for frequency analysis of a rotating conical shell with initial pressure. Int J Numer Methods Eng 48:1703–1722. https://doi.org/10.1002/1097-0207(20000830)48:12%3c1703::aid-nme961%3e3.0.co;2-x

54. Viola E, Artioli E (2004) The G. D. Q. method for the harmonic dynamic analysis of rotational shell structural elements. Struct Eng Mech 17:789–817. https://doi.org/10.12989/sem.2004.17.6.789

55. Artioli E, Viola E (2005) Static analysis of shear-deformable shells of revolution via G.D.Q. method. Struct Eng Mech 19:459–475. https://doi.org/10.12989/sem.2005.19.4.459

56. Artioli E, Gould PL, Viola E (2005) A differential quadrature method solution for shear-deformable shells of revolution. Eng Struct 27:1879–1892. https://doi.org/10.1016/j.engstruct.2005.06.005

57. Irie T, Yamada G, Muramoto Y (1984) Free vibration of joined conical-cylindrical shells. J Sound Vib 95:31–39. https://doi.org/10.1016/0022-460X(84)90256-6

58. Kamat S, Ganapathi M, Patel BP (2001) Analysis of parametrically excited laminated composite joined conical-cylindrical shells. Comput Struct 79:65–76. https://doi.org/10.1016/S0045-7949(00)00111-5

59. Lee YS, Yang MS, Kim HS, Kim JH (2002) A study on the free vibration of the joined cylindrical-spherical shell structures. In: Computers and Structures. Pergamon, pp 2405–2414

60. Wu S, Qu Y, Hua H (2013) Vibration characteristics of a spherical-cylindrical-spherical shell by a domain decomposition method. Mech Res Commun 49:17–26. https://doi.org/10.1016/j.mechrescom.2013.01.002

61. Bagheri H, Kiani Y, Eslami MR (2017) Free vibration of joined conical-conical shells. Thin-Walled Struct 120:446–457. https://doi.org/10.1016/j.tws.2017.06.032

62. Bagheri H, Kiani Y, Eslami MR (2018) Free vibration of joined conical–cylindrical–conical shells. Acta Mech 229:2751–2764. https://doi.org/10.1007/s00707-018-2133-3

63. Li H, Cong G, Li L et al (2019) A semi analytical solution for free vibration analysis of combined spherical and cylindrical

shells with non-uniform thickness based on Ritz method. Thin-Walled Struct 145:106443. https://doi.org/10.1016/j.tws.2019.106443

64. Pang F, Li H, Cui J et al (2019) Application of flügge thin shell theory to the solution of free vibration behaviors for spherical-cylindrical-spherical shell: a unified formulation. Eur J Mech A/Solids 74:381–393. https://doi.org/10.1016/j.euromechsol.2018.12.003

65. Rezaiee-Pajand M, Sobhani E, Masoodi AR (2021) Semi-analytical vibrational analysis of functionally graded carbon nanotubes coupled conical-conical shells. Thin-Walled Struct 159:107272. https://doi.org/10.1016/j.tws.2020.107272

66. Qu Y, Wu S, Chen Y, Hua H (2013) Vibration analysis of ring-stiffened conical-cylindrical-spherical shells based on a modified variational approach. Int J Mech Sci 69:72–84. https://doi.org/10.1016/j.ijmecsci.2013.01.026

67. Xie K, Chen M, Li Z (2017) Free and Forced Vibration Analysis of Ring-Stiffened Conical-Cylindrical-Spherical Shells Through a Semi-Analytic Method. J Vib Acoust Trans ASME 139:. https://doi.org/10.1115/1.4035482

68. Zhao Y, Shi D, Meng H (2017) A unified spectro-geometric-Ritz solution for free vibration analysis of conical–cylindrical–spherical shell combination with arbitrary boundary conditions. Arch Appl Mech 87:961–988. https://doi.org/10.1007/s00419-017-1225-1

69. Bendenia N, Zidour M, Bousahla AA, et al (2020) Deflections, stresses and free vibration studies of FG-CNT reinforced sandwich plates resting on Pasternak elastic foundation. Comput Concr 26:213–226. https://doi.org/10.12989/cac.2020.26.3.213

70. Bourada F, Bousahla AA, Tounsi A, et al (2020) Stability and dynamic analyses of SW-CNT reinforced concrete beam resting on elastic-foundation. Comput Concr 25:485–495. https://doi.org/10.12989/cac.2020.25.6.485

71. Bousahla AA, Bourada F, Mahmoud SR, et al (2020) Buckling and dynamic behavior of the simply supported CNT-RC beams using an integral-first shear deformation theory. Comput Concr 25:155–166. https://doi.org/10.12989/cac.2020.25.2.155

72. Heidari FKMMA (2021) On the mechanics of nanocomposites reinforced by wavy/defected/aggregated nanotubes. Steel Compos Struct 38:533–545. https://doi.org/10.12989/SCS.2021.38.5.533

73. Zerrouki R, Karas A, Zidour M, et al (2021) Effect of nonlinear FG-CNT distribution on mechanical properties of functionally graded nano-composite beam. Struct Eng Mech 78:117–124. https://doi.org/10.12989/sem.2021.78.2.117

74. Rafiee M, Liu XF, He XQ, Kitipornchai S (2014) Geometrically nonlinear free vibration of shear deformable piezoelectric carbon nanotube/fiber/polymer multiscale laminated composite plates. J Sound Vib 333:3236–3251. https://doi.org/10.1016/j.jsv.2014.02.033

75. Ebrahimi F, Habibi S (2018) Nonlinear eccentric low-velocity impact response of a polymer-carbon nanotube-fiber multiscale nanocomposite plate resting on elastic foundations in hygrothermal environments. Mech Adv Mater Struct 25:425–438. https://doi.org/10.1080/15376494.2017.1285453

76. Gholami R, Ansari R (2018) Nonlinear bending of third-order shear deformable carbon nanotube/fiber/polymer multiscale laminated composite rectangular plates with different edge supports. Eur Phys J Plus 133:1–14. https://doi.org/10.1140/epjp/i2018-12103-2

77. Dabbagh A, Rastgoo A, Ebrahimi F (2019) Finite element vibration analysis of multi-scale hybrid nanocomposite beams via a refined beam theory. Thin-Walled Struct 140:304–317. https://doi.org/10.1016/j.tws.2019.03.031

78. Karimiasl M, Ebrahimi F, Mahesh V (2019) Nonlinear free and forced vibration analysis of multiscale composite doubly curved

shell embedded in shape-memory alloy fiber under hygrothermal environment. JVC/Journal Vib Control 25:1945–1957. https://doi.org/10.1177/1077546319842426

79. Jalaei MH, Civalek (2019) On dynamic instability of magnetically embedded viscoelastic porous FG nanobeam. Int J Eng Sci 143:14–32. Doi: https://doi.org/10.1016/j.ijengsci.2019.06.013

80. Arefi M, Kiani M, Civalek O (2020) 3-D magneto-electro-thermal analysis of layered nanoplate including porous core nanoplate and piezomagnetic face-sheets. Appl Phys A Mater Sci Process 126:1–18. https://doi.org/10.1007/s00339-019-3241-1

81. Arshid E, Khorasani M, Soleimani-Javid Z et al (2021) Porosity-dependent vibration analysis of FG microplates embedded by polymeric nanocomposite patches considering hygrothermal effect via an innovative plate theory. Eng Comput. https://doi.org/10.1007/s00366-021-01382-y

82. Hadji L, Avcar M (2021) Nonlocal free vibration analysis of porous FG nanobeams using hyperbolic shear deformation beam theory. Adv Nano Res 10:281–293. https://doi.org/10.12989/anr.2021.10.3.281

83. Hadji L, Avcar M (2021) Free Vibration Analysis of FG Porous Sandwich Plates under Various Boundary Conditions. J Appl Comput Mech 7:505–519. https://doi.org/10.22055/jacm.2020.35328.2628

84. Ramteke PM, Panda SK (2021) Free Vibrational Behaviour of Multi-Directional Porous Functionally Graded Structures. Arab J Sci Eng 1–16. https://doi.org/10.1007/s13369-021-05461-6

85. Ramteke PM, Mehar K, Sharma N, Panda SK (2021) Numerical prediction of deflection and stress responses of functionally graded structure for grading patterns (power-law, sigmoid, and exponential) and variable porosity (even/uneven). Sci Iran 28:811–829. https://doi.org/10.24200/SCI.2020.55581.4290

86. Sancaktar E, Asiri AY, Kumar GS (2004) A novel economical method to improve the toughness of carbon/epoxy long fiber components by the integration of tow loops cores. In: American society of mechanical engineers, design engineering division (Publication) DE. American Society of Mechanical Engineers (ASME), pp 173–188

87. Magnucki K, Stasiewicz P (2004) Elastic buckling of a porous beam | Magnucki | Journal of Theoretical and Applied Mechanics. J Theor Appl Mech 46:333–337

88. Magnucka-Blandzi E (2008) Axi-symmetrical deflection and buckling of circular porous-cellular plate. Thin-Walled Struct 46:333–337. https://doi.org/10.1016/j.tws.2007.06.006

89. Jabbari M, Mojahedin A, Khorshidvand AR, Eslami MR (2014) Buckling analysis of a functionally graded thin circular plate made of saturated porous materials. J Eng Mech 140:287–295. https://doi.org/10.1061/(asce)em.1943-7889.0000663

90. Nieto A, Boesl B, Agarwal A (2015) Multi-scale intrinsic deformation mechanisms of 3D graphene foam. Carbon N Y 85:299–308. https://doi.org/10.1016/j.carbon.2015.01.003

91. Wang C, Zhang C, Chen S (2016) The microscopic deformation mechanism of 3D graphene foam materials under uniaxial compression. Carbon N Y 109:666–672. https://doi.org/10.1016/j.carbon.2016.08.084

92. Qin Z, Jung GS, Kang MJ, Buehler MJ (2017) The mechanics and design of a lightweight three-dimensional graphene assembly. Sci Adv 3:e1601536. https://doi.org/10.1126/sciadv.1601536

93. Khan M, Wang C, Wang S, et al The mechanical property and microscopic deformation mechanism of nanoparticle-contained graphene foam materials under uniaxial compression. iopscience.iop.org

94. Tsai SW (1964) Structural Behavior of Composite Materials. Philco Corp Newport Beach CA

95. Tsai SW (1965) Strength Characteristics of Composite Materials. Philco Corp Newport Beach CA

96. Tsai SW, Adams DF, Doner DR (1966) Analyses of Composite Structures. Philco Corp Newport Beach CA

97. Halpin JC (1969) Effects of environmental factors on composite materials. Air Force Materials Lab Wright-Patterson AFB OH

98. Affdl JCH, Kardos JL (1976) The Halpin-Tsai equations: A review. Polym Eng Sci 16:344–352

99. Reddy JN (2003) Mechanics of Laminated Composite Plates and Shells Theory and Analysis

100. Rezaiee-Pajand M, Sobhani E, Masoodi AR (2020) Free vibration analysis of functionally graded hybrid matrix/fiber nanocomposite conical shells using multiscale method. Aerosp Sci Technol 105:105998. https://doi.org/10.1016/j.ast.2020.105998